ADVANCED ENGINEERING MATERIALS
www.aem-journal.com

Review on Strain Localization Phenomena Studied by High-Resolution Digital Image Correlation

Anja Weidner and Horst Biermann*

Herein, a comprehensive review on the application of digital image correlation (DIC) for investigations of strain localization phenomena in the field of materials science and engineering (MSE) is provided. The Review is divided into three parts. In Part 1, the method of DIC is reviewed in terms of basic principles, correlation algorithms, and sources of errors. Part 2 is focused on the application of DIC in the field of MSE. This part is subdivided into the application of DIC in 1) combination with optical microscopy and 2) in combination with scanning electron microscopy (SEM). In Part 3, results of high-resolution DIC obtained in combination with SEM are presented for high-strength austenitic stainless steels—transformation-induced plasticity steels and twinning-induced plasticity steels—exhibiting microscopic strain localization phenomena. These investigations are supplemented by electron backscattered diffraction for interpretation of strain fields. Although DIC allows for both 2D and 3D calculations of displacement and strain fields, herein, 2D digital correlation is referred to only, as in particular with SEM only in-plane displacements are calculated so far.

1. Introduction

Localization of strain is a well-known phenomenon that occurs under various loading conditions such as uniaxial and multiaxial, monotonic and cyclic loading, as well as high-speed deformation in a broad variety of materials such as ductile single crystals, polycrystalline materials with various grain sizes down to nanocrystalline materials, and metallic glasses. Strain localizations may appear on different length scales ranging from the macroscale to the meso- and microscale and can be distinguished into stationary and propagative strain localizations.

In general, strain localizations are the consequence of the loss of uniform deformation causing plastic instabilities and are related, consequently, with an inhomogeneous deformation at the dislocation scale. Typical types of strain localizations are 1) formation of slip bands, deformation bands, or persistent slip bands during cyclic deformation, 2) development of shear bands, 3) features of dynamic strain aging such as propagating Lueders bands or Portevin Le Chatelier (PLC) bands, 4) formation of a plastic zone in front of a crack tip, or 5) the most common strain localization of ductile materials—i.e., necking. The well-known criterion of necking is the Considère criterion (or h-type criterion,[1] which is related to strain hardening. Another criterion of plastic instability is the so-called S-type criterion,[2,3] which is related to strain rate sensitivity yielding, e.g., the PLC effect. The T-type instability criterion[2,3] is related to the heat equation describing the interaction between strain rate and temperature increase and is mainly observed in case of the formation of adiabatic shear bands. Research on plastic strain localizations has been the focus of an incredibly huge number of investigations. In the past, several review papers were concerned with summarizing different aspects of strain localizations (e.g., studies by Rice,[4] Brechet and Louchet,[5] and Antolovich and Armstrong[6]).

Excellent methods for the characterization of strain localizations related to different instability criteria and different length scales are the so-called full-field measuring techniques —digital image correlation (DIC) invented in the early 1980s and infrared thermography (IR-TG) used in materials research since the early 1990s. Whiles DIC provides 2D and 3D displacement/strain fields, IR-TG provides temperature fields. The combination of these methods in terms of full-coupled full-field techniques allows, therefore, a comprehensive understanding of strain localization phenomena related to different instability criteria. These techniques yield a wealth of data, which are superior to classic measurement methods, such as strain gauges or thermocouples providing only a limited amount of data for comparison and disregarding the possible heterogeneity of displacement or thermal fields.[7]

The DIC technique is one of the most often applied optical and contactless methods for measurements of displacements on a wide scale—from the macrometer scale down to the micrometer and even submicrometer scale—using both 2D DIC (e.g., scanning electron microscopy [SEM],[8–12] focused ion beam [FIB] technique,[13–15] or atomic force microscopy [AFM][16–21]) and 3D DIC.[22–24] The application of DIC technique in combination

Dr. A. Weidner, Prof. H. Biermann
Institute of Materials Engineering
Technische Universität Bergakademie Freiberg
Gustav-Zeuner-Str. 5, Freiberg 09599, Germany
E-mail: weidner@ww.tu-freiberg.de

The ORCID identification number(s) for the author(s) of this article can be found under https://doi.org/10.1002/adem.202001409.

DOI: 10.1002/adem.202001409

with high-spatial-resolution imaging methods like optical microscopy (OM) including confocal laser scanning microscopy (CLSM), SEM, transmission electron microscopy (TEM),[25] AFM, FIB technology, and computer tomography (CT) was in the past attractive.

A challenging task for all DIC applications is the preparation of a suitable surface pattern contrast, which is closely related to the material under investigation and the conducted experiment. The aim of all contrasting methods is to achieve a randomly distributed, well-contrasted speckle pattern down to nanometer size for both high spatial and strain resolution of DIC calculations. The contrast techniques range from application of nanosized particles on the surface over electron beam-induced or vapor-induced deposition processes of particles up to techniques like etching or FIB milling.

The combination of quasi-in situ experiments in SEM with the DIC technique is a powerful method which can be completed with additional techniques such as electron backscattered diffraction (EBSD) to evaluate the formation of strain localizations. However, DIC in combination with SEM images holds some challenges. Due to the scanning character of the SEM, the recorded SEM micrographs can yield a complex image distortion consisting of spatial and drift distortion.[12] Depending on the dwell time, magnification, and loading conditions, the capture of spatial and drift distortions is more distinct. Several research groups[26,27] published distortion correction procedures, in particular for the specific problems of displacement correlation with SEM micrographs.

The earlier-mentioned instability criteria and the consequently resulting strain localizations are also since long time in the focus of numerical simulations. Thus, different numerical procedures/approaches are under development. These models were developed at multiple length scales ranging from structural scale over macro-, meso-, and microscale down to the atomic and electronic level[28] including finite element modeling (FEM), crystal plasticity (CP) modeling, phase field (PF) modeling, discrete dislocation dynamics (DDD) modeling, molecular dynamic (MD) modeling, and density functional theory (DFT) modeling. These approaches should enable researchers and engineers to identify constitutive parameters and, in particular, estimate as many parameters as possible using as few experiments as necessary. Finally, the parameter identification from few model experiments would be beneficial for the approach of multiscale modeling in the field of Integrated Computational Materials Engineering (ICME), in particular for the top-down approach from models for macroscale plasticity down to atomistic and/or DDD simulations.[29] For example, a novel integrative experimental–numerical approach in the field of metals plasticity was offered quite recently by Tasan et al.[30] The physically based models in Düsseldorf Advanced Materials Simulation Kit (DAMASK)[31] are substantially supported by the incorporation of data describing the stress and strain partitioning during plastic deformation of dual-phase (DP) steel obtained from a combination of in situ deformation in SEM with EBSD, DIC, and FIB. In addition, local strain and stress distributions were revealed from 2D CP simulations corroborated by additional inverse simulations of nanoindentation measurements of the initial microstructure. Another example was presented by Song et al.[32] for the formation of bainite in the steel 100Cr6 using ab initio calculations and PF modeling in combination with advanced characterization techniques such as atom probe tomography (APT) and TEM. As a third example, the recently published approach of Hosdez et al.[33] demonstrates the coupling of an elastic-plastic FEM model and experimental measurements of displacements using DIC for the investigation of the evolution of the plastic zone during fatigue crack growth in a cast iron with spheroidal graphite. The coupling of FEM and DIC combines the accuracy and the large amount of information provided by DIC with the wide possibility range of FEM. The measured displacement fields were used as boundary conditions in elastic-plastic computations. This allows to apply cycles between each new boundary condition to be close to reality and observe the plasticity evolution from small-to-large-scale-yielding conditions. However, the DIC–FEM approach does not consider the plain stress/strain hypothesis yielding curved crack shapes. As a possible way out of this restriction, the coupling of CT and 3D FEM was postulated, which seems to be promising for cast iron due to the excellent contrast between graphite and iron.[33]

The aim of the Review is twofold. On one hand, the Review highlights the richness, versatility, and usefulness of full-field measurements using DIC for investigations of strain localization phenomena in the field of materials science and engineering (MSE). On the other hand, the Review highlights the high-resolution DIC in combination with in situ SEM deformation experiments for the investigation of strain localizations on microscopic scale. Here, the definition of high-resolution is related both to the lateral resolution and to the strain resolution of the strain fields obtained by DIC calculations. The Review is, therefore, focused on 2D DIC solely. The Review is divided into three parts. In Part 1, the method of DIC is reviewed in terms of basic principles, correlation algorithms, and sources of errors. Part 2 is focused on the application of DIC in the field of MSE. This part is subdivided into application of DIC in 1) combination with OM and 2) in combination with SEM. In part 3, case studies are presented where DIC is applied in combination with SEM on microscopic strain localizations occurring in high-strength austenitic stainless steels. This part presents results from in situ experiments with a scanning electron microscope under tensile loading at different temperatures in combination with calculations of local strain fields using DIC supplemented with EBSD for interpretation of strain fields. The material under investigation is a class of high-alloy, high-strength steels—the so-called transformation-induced plasticity (TRIP) steels and twinning-induced plasticity (TWIP) steels. In situ SEM–μDIC experiments were conducted on three steels with different nickel contents and at different deformation temperatures to vary the austenite stability and the stacking fault energy (SFE). The surface contrast pattern was achieved by an etching process which caused a fine-structured contrast pattern allowing for spatial resolution in the submicrometer scale. The μDIC results were correlated with results from EBSD measurements and detailed slip-system analyses. Finally, the magnitudes of shear of individual microstructural constituents such as deformation bands, twins, or α'-martensite were experimentally evaluated for the first time. In the end, the achieved lateral and strain resolution as well as the influence of grain size is discussed.

Table 1. Summary of possible imaging methods, their intensity information, and typical image resolution parameters applicable for DIC measurements.

No.	Imaging method	Obtained intensity information	Typical imaging parameter (resolution)
1	Video records of CCD cameras digitized by frame grabber cards	Light intensity (grayscale), also infrared, ultraviolet, ionizing radiation (X-ray) depending on used camera or detector	CCIR Video standard norm: 752 × 582 pixels; high-resolution CCD cameras: 1300 × 1300 pixels or higher
2	Commercial digital camera	Light intensity (grayscale)	1300 × 1030 pixels up to several *k*-pixels × *k*-pixels
3	Scans of photographs	Light intensity (grayscale), also infrared, ultraviolet, ionizing radiation (X-ray) depending on used camera or detector	Depending on used scanner device, up to $10^5 \times 10^5$ pixels
4	Electron microscopy (including FIB technology)	Electron beam current, SE contrast, BSE contrast, element analytic contrast	512 × 512 pixels up to 4096 × 4096 pixels or higher
5	Scanning tunneling microscopy	Tunnel or distance signal	512 × 512 pixels up to 4096 × 4096 pixels
6	AFM	Force or distance signal	512 × 512 pixels up to 4096 × 4096 pixels
7	Laser scanning microscopy	Light intensity (grayscale), height information, luminescence signal	512 × 512 pixels up to 4096 × 4096 pixels or higher
8	IR-TG	Intensity of infrared radiation	240 × 1240 pixels or higher

In addition, the manuscript is complemented by Supporting Information regarding both a historical overview on DIC applications in the past 20 years and supporting videos for SEM–μDIC applied on metastable austenitic stainless steels.

2. Basics on DIC

2.1. Short History

In the 1970s and 1980s, a series of optical methods was established for measurements of macroscopic properties such as displacements and strains. According to Grediac and Hild,[34] 1) interferometric methods, 2) grid methods, and 3) image correlation methods can be distinguished. In addition to these numerical methods, also direct methods like 1) shearography and 2) speckle-shearing photography are known. Among the interferometric methods, 1) holographic (e.g., ref. [35]), 2) speckle (e.g., ref. [36]), 3) and Moiré interferometry (e.g., refs. [37,38]) allowed for both in-plane and out-of-plane displacements. While holographic interferometry is based on the analysis of interference fringes produced by superimposing a reference hologram image on specimens subjected to subsequent deformation, speckle interferometry uses relative phase changes due to interference of two coherent light fields of random phase and amplitude. Moiré interferometry uses grating structures on specimen surfaces, and a superposition of a reference pattern of an undeformed state with a pattern in the deformed state resulting in the so-called Moiré fringe pattern[37,39] is applied. However, besides the high requirements on the temporal and thermal stability of the experimental setups, the most important drawback of all these interferometric techniques is the laborious and time-consuming analysis of the fringe patterns demanding an automated pattern recognition and analysis.[34]

In the beginning of the 1980s, the method of DIC was introduced by researchers of the University of South Carolina.[40,41] Thus, Sutton et al.[40] and Chu et al.[41] developed this technique to measure displacements of objects under loading conditions with high accuracy. Since the invention of DIC in 1983, it is defined as an optical, contactless, noninvasive measuring technique. The aim of DIC is to calculate both in-plane 2D and out-of-plane 3D displacement fields of specimens, structures, or components. The method is based on digital images at different loading conditions such as 1) mechanical, 2) thermal, or 3) chemical loading, as it is fairly tolerant to several experimental conditions. Digital images from different sources providing grayscale (or false-colored) images can be used. **Table 1** shows a summary of possible imaging methods used for both 2D and 3D DIC together with achievable information content and possible resolution. The use of a large variety of imaging methods opened a wide field of application of DIC in the fields of MSE, experimental mechanics, safety engineering, and geological science.

In MSE and experimental mechanics, DIC is meanwhile a very popular and powerful method for measuring surface displacements in a wide range of applications from the macroscale down to the submicrometer scale. In materials research, DIC is an appropriate method for combination with any other microscopic technique used for in situ characterization experiments such as OM (e.g., refs. [42–45]), SEM (e.g., refs. [8–11,46]), FIB technique (e.g., refs. [13–15]), or AFM (e.g., refs. [16–21]). Together with IR-TG, it can be applied for so-called fully coupled full-field measurements (e.g., refs. [47–51]) or infrared image correlation (IRIC).[52] The application of multicamera systems allows for 3D DIC. Computer-tomographic experiments (e.g., refs. [22–24]) can provide displacements using the so-called digital volume correlation (DVC).

In the following sections, the principle of DIC (Section 2.2), the correlation algorithms (Section 2.3), the image pattern contrast (Section 2.4), the presentation of 2D strain values (Section 2.5) as well as sources of errors of DIC calculations (Section 2.6) will be tightly summarized.

2.2. Principle of DIC

The principle of DIC is described in numerous publications (e.g., ref. [53]. The goal of DIC is the evaluation of the sought mechanical transformation Φ between the reference image f and the image of deformed state g according to Equation (1)[34]:

$$g(\Phi(x)) = f(x) \tag{1}$$

The principle of DIC is shown in **Figure 1**. Both the reference image f and the image g are digital images of an area of interest (AOI). These digital images should have a characteristic contrast pattern with a defined speckle dimension related to the desired resolution of the strain field measurements. In the first step, an equidistant grid of measuring points p (blue in Figure 1a) is defined in an AOI on the specimen surface according to a predefined specimen coordinate system (x,y,z). Each point is given by two coordinates i and j related to the x and y direction, respectively, of the specimen coordinate system (Figure 1b). In the second step, a subset (black in Figure 1a,b) of the size $n \times n$ (square shaped) or $m \times n$ (rectangular shaped) is defined surrounding each measuring point.

The size of the subset has to be defined with respect to the present speckle dimensions, the image resolution of the used camera device, and the desired resolution of the DIC calculations. In addition, each measuring point and subset is accompanied by a search field (yellow in Figure 1b,c) of the size $N \times N$ (square shaped) or $M \times N$ (rectangular shaped). The size of the search field has to be adopted to both the size of the subset and the applied loading conditions and material behavior. In particular, rectangular search fields are highly recommended in the case for large strain deformation in tension of ductile materials to compensate for the strong rigid-body motion. Each subset in AOI of the reference image is characterized by—in the best case—a unique speckle pattern. The basic principle of DIC is to track this unique speckle pattern of each subset in both images—reference image f and image g of the deformed state (compare Figure 1b,c). The subset with the identical speckle pattern is now found at the position point $p_{i'j'}$ (red in Figure 1c), which is characterized by a displacement of i' in x direction and j' in y direction. The indicated white arrow in Figure 1c is then the displacement vector from point $p_{i,j}$ in reference image f to point $p_{i'j'}$ in image g. Thus, for all points within the reference subset, a displacement vector can be obtained, as neighbor relationships within one individual subset remain unchanged. However, the shape of the target subset can change during deformation depending on differences in local displacements. Besides the rigid-body translations between reference image f and image g, shape functions of first and second order have to be considered related to local stretching, shearing, and rotating operations of measuring points or their combinations.

2.3. Cross-Correlation Algorithm, Subpixel Accuracy, and Heavyside DIC

The principle of DIC is based on the comparison of the gray value distribution of a speckle pattern in a reference subset and a target subset. Where the similarity/match in the image g is greatest, the displacement vector of a measuring point is identified. The degree of similarity/matching is determined by a correlation algorithm. In literature, mainly two different approaches are known: 1) the cross-correlation (CC) algorithm and 2) the sum of squared differences (SSD) algorithm.[54,55] While the first one is based on the maximization of the similarity/matching between the grayscale distribution of reference subset image f and target subset image g, the SSD algorithm is based on the minimization of the differences between both subsets.[54] Both for CC and SSD algorithms, 1) standard, 2) normalized, or 3) zero-normalized procedures are known. The difference between these three different procedures is which types of values are used for determining the similarities (CC) or differences (SSD). Thus, the standard method uses the absolute values of grayscale levels, whereas the zero-normalized procedure sets the average grayscale difference or similarity to zero and uses then the global variation in the grayscale.[56] Pan et al.[56] concluded that the zero-normalized CC (ZNCC) provides the most robust noise performance and is insensitive to an offset and a linear scale in illumination lighting. In contrast, the normalized procedures (NCC and normalized sum square difference [NSSD]) are insensitive to a linear scale in illumination lighting but sensitive to an offset of lighting: The standard procedures (CC and SSD) are sensitive to all lighting fluctuations. The most

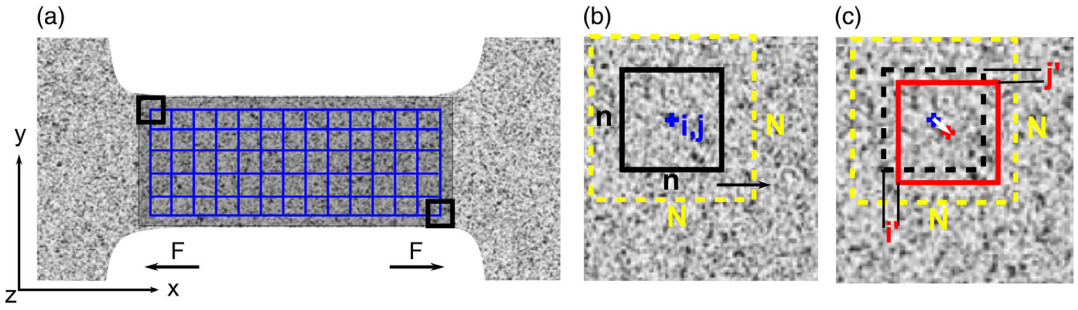

Figure 1. Principle of DIC. a) Definition of a grid of measuring points (blue) in an AOI (dark gray area) on the specimen's surface with respect to the predefined specimen coordinate system (x,y,z). b) Reference image f with speckle pattern, measuring point $p_{i,j}$ (blue cross), subset (black) of size $n \times n$, and search field (yellow) of size $N \times N$. c) Image g of deformed state with the original measuring point $p_{i,j}$ (blue) and reference subset (black) and the displaced measuring point $p_{i'j'}$ (red) with target subset (red) and displacements i' and j' in x- and y-directions, respectively. White arrow shows the displacement vector. Partly reproduced with permission.[141] Copyright 2020, Springer.

commonly used criterion in commercially available software packages is, therefore, the ZNCC algorithm.[56] Thus, the CC coefficient C is calculated for all possible measuring positions of a subset $n \times n$ in the search field $N \times N$. To this end, a 2D field of CC coefficients having a discrete maximum $C_{max,disc}$ will be obtained for each displacement i' and j'. Finally, the subset in the reference image f will shift to the position of $C_{max,disc}$ in the target subset of image g. The correlation coefficient scales are in the range $0 \leq C \leq 1$, where $C = 0$ is related to no match between reference and target subset and $C = 1$ to perfect match. For good displacement calculations $C > 0.5$ should be achieved.

However, the smallest unit of a digital image is one single pixel. Therefore, the accuracy of the calculated displacement is limited to a multiple-integer pixel. The enhancement of accuracy of displacement calculations can be achieved by three different possibilities: 1) enhancement of camera resolution, 2) enlargement of magnification, and 3) the implementation of a subpixel registration algorithm to the DIC calculations. The first two methods are the so-called direct methods and are useful for a 1) fixed field of view (FOV) or are accompanied by a 2) reduction of FOV. The "subpixel registration" algorithm is an indirect method but very effective. In the literature, at least three different approaches for the subpixel algorithm are known: 1) the correlation coefficient curve-fitting method,[57] 2) the Newton–Raphson method,[58] and 3) the gradient-based method, which was introduced by David and Freemann as a method of optical flow.[59] An overview on all three methods is given by Pan et al.[57] The correlation coefficient curve-fitting method describes the correlation coefficient field C_{x_i,y_j} for a pixel P with the coordinates (x, y) and its eight neighbors $P_{i,j}$ with the coordinates $(x_i y_j)$ as a fitting surface using 2D quadratic functions. For the calculation of the displacement of the field of CC coefficients, a set of linear equations has to be solved. Finally, a displacement accuracy below one pixel will be achieved.

Recently, an improved DIC code was developed by Bourdin et al.[60] considering also kinematical discontinuities—the so-called "Heavyside-DIC (H-DIC)". In addition to the conventional DIC method, this method includes a so-called jump or step function U' and the Heavyside function H. While the jump function U' describes the magnitude of the kinematical discontinuity in horizontal and vertical directions, the Heavyside function H describes the precise location of the discontinuity at any orientation and displacement from the subset center. The location of discontinuity is described by polar coordinates r^* and Θ^*, where r^* is related to the minimum distance between the discontinuity and the center of the subset and Θ^* is the angle of discontinuity inside the subset. The Heavyside function allows then to identify two parts of a subset, which are affected (or not) by a discontinuity/jump, and shift one side of the subset with respect to the other one by the magnitude of the jump. The application of this new approach of the improved DIC code allows for discontinuity-tolerant, quantitatively, and statistically confirmed investigations of plasticity at the scale of individual slip systems (SSs) both during quasistatic loading and during cyclic loading, as shown for a nickel-base superalloy by Bourdin et al.[60] and Stinville et al.,[61] respectively.

2.4. Image Pattern Contrast for DIC

A suitable pattern contrast at the surface of the investigated specimen is an essential condition for the successful correlation of the reference image f and the image g of the deformed state. First of all, the contrast pattern must have a characteristic signature for each surface element, which is transported simply by displacement and which can follow deformation without further impairment/changes or deterioration.[34] The digital images obtained from different techniques (see Table 1) provide mostly grayscale images or in case of AFM and TG also false-colored images. These images should have a broad dynamic range. Thus, in case of grayscale images, the gray levels should cover as much as possible of the available range of the encoding depth of the images (e.g., 256 levels for 8-bit images and 4096 levels for 16-bit images). Any saturation at the lower or upper bound of this range should be avoided.[34] A good sensitivity, in particular for small displacement amplitudes, is achieved by a strong contrast between two neighboring pixels.

In general, an artificial pattern contrast is applied to the specimen surface. To this end, several methods are available: 1) speckle pattern, 2) deposition of particles, 3) etching technique, and 4) grid technologies.

1) The "speckle pattern technique" uses fine powder particles of black paint sprayed on a white background. A fine aerosol of the paint is obtained using airbrush technology. The size of paint droplets can be adjusted by a nozzle. The obtained speckle pattern has to meet high requirements both regarding the speckle dimensions and the speckle distribution. In the best case, the black droplets are arranged randomly, the contrast covers a wide dynamic range, and there are sharp contrast changes between individual pixels. The application of the speckle pattern for DIC covers a wide range of specimen dimensions up to large-scale components in combination with all-optical-microscopic image-recording techniques like a digital camera, high-speed camera, long-distance microscope, and confocal laser scanning microscope. However, the application of a speckle pattern is limited by the testing conditions. Thus, large deformations and/or the combination with high temperature can result in the damage and failure of the paint layer. Consequently, this yields a loss of correlation between reference image f and image of deformed state g. A possibility for large deformations could be the application of metal powder. However, for DIC analysis in combination with SEM, the speckle paint pattern technology is unfavorable and one of the three other techniques described in the following is more convenient.

2) The "deposition of particles" is a method which is mostly used in combination with SEM. Fine particles of precious metals (gold, silver) with a size in the nanometer range were deposited on the specimen surface by the vapor-assisted remodeling of thin metal films. Thus, Luo et al.[62] exposed ultrathin gold films (<20 nm) from condensable vapors of volatile solvents at relatively low temperatures (60–120 °C), which resulted in spherical gold nanoparticles with diameters between about 100 to 500 nm depending on the initial thickness of the gold layer and the vapor exposure. This method was improved and enhanced by Scrivens et al.[63] to a broad variety of substrate materials (e.g., glass, silicone rubber, epoxy resin, aluminum, silicon, stainless steel), as

well as different patterned metal films (e.g., chromium, copper, silver, combined gold, and silver). Finally, Scrivens et al.[63] obtained particle sizes between 25 and 500 nm. A further method for deposition of nanosized particles is thorough thin-film ablation (TTFA) by laser techniques.[64] The apparent drawbacks of these technologies are the connectivity of the nanoparticles to specimen surface, the pattern stability at elevated temperatures, and possible agglomeration of particles.

3) The well-established technique of "etching" is one of the best methods to obtain a randomly distributed and small-sized contrast pattern on the specimen surface (e.g., ref. [10]). Fine etch pits were obtained depending on the materials under investigation. The benefit of this technique is the durability of the etch pit pattern during the entire (even large) plastic deformation process even at higher temperatures.

4) The "grid technology" is based on the application of microgrids onto the specimen surface. These microgrids can be obtained by different techniques such as 1) electron beam lithography (e.g., ref. [65]) and 2) deposition of gold or other precious metals on a nickel grid glued onto the specimen surface (e.g., ref. [66]). The challenge of grid technology is to find a compromise between line width and mesh size of the grid regarding accuracy of measurements and the size of the observed field.[67]

However, in some cases, even the natural structure of the studied material can be sufficient for sensitive correlation results like 1) two-phase microstructures (e.g., DP steel,[68] Ni-base superalloys[64,69,70]), 2) layered microstructures (e.g., Al laminates produced by accumulative roll bonding[42]), and 3) meshed structures produced by powder-bed fusion additive manufacturing (e.g., selective laser melting or electron beam melting of TiAl6V4 alloy,[44,71] respectively). However, the main drawback here could be preferred orientation of the natural pattern (e.g., layered arrangements of two phases in duplex stainless steel).

2.5. Presentation of 2D DIC results

The first outcomes of 2D DIC are in-plane displacement vectors. Thus, a displacement vector will be obtained in the image of g of the deformed state for each measuring point. The entirety of in-plane displacements is given by the second-order displacement tensor U. In analogy with the displacement tensor U, the second-order strain tensor ε can be calculated and is given in Equation (2)[72]

$$\varepsilon = \begin{pmatrix} \varepsilon_{11} & \varepsilon_{12} \\ \varepsilon_{21} & \varepsilon_{22} \end{pmatrix} = \begin{pmatrix} \varepsilon_{xx} & \varepsilon_{xy} \\ \varepsilon_{yx} & \varepsilon_{yy} \end{pmatrix} = \begin{pmatrix} \frac{\partial u_x}{\partial x} & \frac{\partial u_x + \partial u_y}{\partial x} \\ \frac{\partial u_x + \partial u_y}{\partial y} & \frac{\partial u_y}{\partial y} \end{pmatrix} \tag{2}$$

Here, u is the displacement in x- and y-direction, respectively. Consistent with the definition of normal stresses and shear stress, ε_{xx} and ε_{yy} are the normal strains acting perpendicular to a face element in x- and y-direction, respectively, whereas ε_{xy} is the shear strain acting parallel to a face element. Considering the resolved strain, different strain (deformation) theories can be applied resulting in different strain measures like 1) stretch ratio, 2) engineering strain ε_{eng}, 3) true strain $\varepsilon_{\text{true}}$ or logarithmic strain φ, and 4) Green's strain.[72] The engineering strain with $\varepsilon_{\text{eng}} = \frac{\Delta l}{l_0}$, where l_0 is the initial length and Δl is the change in length, and the true strain with $\varepsilon_{\text{true}} = \ln(1 + \varepsilon_{\text{eng}})$, are most commonly used.

The shear strain ε_{xy} acting parallel to a face element yields a change in the shape of this surface element. This shape change can be described by the shear angle γ_{xy}, which consists of two parts (see Equation (3)), which are not necessarily identical.[72,73]

$$\gamma_{xy} = \frac{\partial u_y}{\partial x} + \frac{\partial u_x}{\partial y} \tag{3}$$

For small strains the strain tensor ε can be then written as[72]

$$\varepsilon = \begin{pmatrix} \varepsilon_{11} & \varepsilon_{12} \\ \varepsilon_{21} & \varepsilon_{22} \end{pmatrix} = \begin{pmatrix} \varepsilon_{xx} & \varepsilon_{xy} \\ \varepsilon_{yx} & \varepsilon_{yy} \end{pmatrix} = \begin{pmatrix} \varepsilon_{xx} & \frac{1}{2}\gamma_{xy} \\ \frac{1}{2}\gamma_{yx} & \varepsilon_{yy} \end{pmatrix} \tag{4}$$

However, $\varepsilon_{xy} = \frac{1}{2}\gamma_{xy}$ is valid only for the small strain theory and not applicable for large plastic deformations. It is obvious from these arguments that a symmetric strain tensor will result only in a parallelogram shape of the strain field, where the orientation of the parallelogram is fixed to the defined coordinate system of the specimen surface (x- and y-direction). Consequently, the displacement tensor U cannot describe the rotation of points. Therefore, the rotation tensor R is necessary, resulting together with the (right-hand) displacement tensor U in the complete transformation tensor F given as[72]

$$F = R \cdot U \tag{5}$$

The rotation tensor R describes both the rotation and the direction of rotations of points. Therefore, in addition to the global coordinate system $(x - y)$, two additional local coordinate systems are necessary: 1) the system $(x' - y')$ describing points in the undeformed state and 2) the system $(x'' - y'')$ related to points in the deformed state. The latter one is independent on rigid-body rotations and translations. The x'' and y'' directions are, therefore, the directions of the normal strain ε_{xx} and ε_{yy}, respectively.[73] Finally, it is obvious that the strain values ε_{xx} and ε_{yy} depend on the coordinate system. To obtain independent strain values, a principal axis transformation of the displacement tensor U can be conducted. As a result, the two eigenvalues λ_1 and λ_2 of the principal axis will be obtained.[72] Depending on the chosen strain measure (ε or φ), the larger eigenvalue corresponds to the major strain ε_1 (φ_1) and the lower eigenvalue to the minor strain ε_2 (φ_2). The related eigenvalue vectors correspond to the directions of major and minor strain, respectively. Along with the major and minor strains, equivalent strains according to the von Mises (ε_{vM}) and Tresca (ε_{T}) approaches may be of interest.[73] All strain values (ε_{xx}, ε_{yy}, ε_{xy}, γ_{xy}, ε_1, ε_2, ε_{vM}, ε_{T}) can be plotted for the AOI as false-color representations. Displacement and rotation vectors can be presented in trajectory plots.

2.6. Sources of Errors in 2D DIC

Possible errors occurring during 2D DIC can be subdivided into three groups: 1) errors related to the experimental setup, 2) errors related to the image pattern contrast, and 3) errors related to the principle of DIC (shape functions, correlation algorithm, subset size). A detailed overview on these errors was given recently by

Zhao et al.[74] At first, the sources of errors will be discussed for the application of optical imaging techniques. At the end of this section, 4) a separate paragraph will discuss errors of DIC in combination with SEM—called SEM–DIC.

1) Errors from experimental setup. Here, the influence of 1) the used camera system, 2) the experimental environment, and 3) the out-of-plane displacement has to be discussed. While the first one can introduce image distortions, the second one has an influence on the noise level in the digital images. The "noise level" of digital images is caused mainly by fluctuations of the illumination and the acquisition hardware resulting in 1) thermal noise, 2) read-out noise, and 3) cut-off noise.[74] In particular, the accuracy of image registration and subpixel interpolation will be influenced by these noises. The application of low-noise camera systems and image averaging can reduce the image noise. Another way is the application of a Gaussian low-pass filter with a kernel of 5×5 pixels to the digital images before the correlation analysis.[75] The influence of fluctuations of the illumination can be encountered by the application of ZNCC or ZNSSD correlation algorithm (see Section 2.2 and point 3) this section). The used camera system can also yield "image distortions" due to lens distortion or self-heating of the digital camera. The effect of lens distortion on the accuracy of DIC calculations can be neglected for macroscopic measurements but is of particular interest at the microstrain scale. However, this effect can be reduced by high-quality lenses in combination with charged coupled device (CCD) sensors. The self-heating of the camera and/or sensor can result in complex image distortions. According to Pan et al.,[75] the application of bitelecentric optics, however, helps to solve the problem of self-heating. Bitelecentric optics are special optical lenses, where the entrance and exit pupil is at infinity, resulting in an orthographic view of the object. Thus, these optics provide the same magnification at all distances and distortion-free images. However, drawbacks of these optics are the fixed FOV and the limited depth in focus. The influence of "out-of-plane displacements" has to be considered, in particular, for 2D DIC. Out-of-plane displacements lead to motion of the investigated specimen surface (both forward and backward translation and rotation) relative to the imaging sensor. In general, the sensitivity to out-of-plane motion is higher, the higher the displacement gradient. For 2D DIC, this effect can be minimized or suppressed also by the application of bitelecentric optics.[75] Otherwise, a multicamera setup can be used for 3D DIC accounting of out-of-plane displacements.

2) Errors related to image pattern contrast. Together with the subset size, the image pattern contrast has the strongest influence on the accuracy of DIC calculations. Therefore, the quality of the image pattern contrast (speckle pattern) has received wide attention and is still a hot topic for researchers. The attractiveness of this topic is related to the following goals: 1) to provide a guide for speckle pattern preparation, 2) to allow a forecast of the accuracy of DIC, and finally, 3) to provide a standard speckle pattern. The performance metrics of speckle patterns can be subdivided into local and global parameters. The local quality of speckle patterns can be assessed, for instance, by the subset intensity gradient, whereas a global indicator could be the mean subset fluctuation.[74] Regarding the object speckle dimensions, it can be stated that the speckle size should be sufficiently small for a good resolution of displacement determination and strain calculation but also sufficiently large to be fully resolved by the used camera system.

3) Errors related to DIC principle. These errors are related to 1) the shape functions, 2) the correlation algorithm, 3) the applied interpolation, and 4) the subset size. Excluding the subset size, all other parameters are inherent to the used commercial DIC software package or have to be reviewed in case of open source software packages or have to be correctly chosen in case of self-written DIC software. As already mentioned in Section 2.1, "shape functions" have to be regarded for the shape change of the target subset in the image of the deformed state g. Zero-order, first-order, and second-order shape functions are known[56]: Zero-order shape functions describe solely rigid-body translations and/or rotations, which means that the displacements are identical for each point within the subset. First-order and second-order shape functions are needed to describe local translations, rotations, normal strains, and shear strains.[26,76,77] The different "correlation algorithms"—CC and SSD—were introduced in Section 2.2. In addition, approaches using the parametric sum of squared differences (PSSD) are known. Here, for instance, two additional parameters a and b accounting for a change in the 1) scale of intensity and 2) change in the offset of intensity in the subset are introduced, leading to so-called PSSDab. Pan et al.[78] showed, in a comparison of ZNCC, ZNSSD, and PSSDab, the robustness and equivalence of the three correlation criteria. Furthermore, the "interpolation" of the intensity plays a significant role in achieving subpixel accuracy of DIC calculations (see Section 2.2). Here, different polynomial interpolation functions like B-spline interpolation or bicubic interpolation are widely used. Gao et al.[12,79] introduced a new method, which allows to capture subpixel shifts by the camera due to the application of integral pixel shifts to the image shown on the screen. The highest impact among the other factors of group (3) is the "subset size." The subset size is, among the other three parameters, the sole, which can be influenced directly by the user of the DIC software. In general, the choice of the subset size is a compromise between the achievable lateral resolution and the precision of the displacement calculations. The lateral resolution of DIC calculations scales directly with the size of the subset—the smaller the subset, higher the lateral resolution. However, too small subset sizes cause miscalculations of displacement vectors as very low lateral information is available. Otherwise, too large subsets will result in systematic errors and are costly in terms of time.

4) Errors related to SEM–DIC. The combination of DIC with in situ deformation in the scanning electron microscope—SEM–DIC—provides a powerful tool for the measurement of 2D, in-plane displacement fields in combination with the characterization of microstructural processes at high lateral resolution.[27,80] However, SEM–DIC is affected by technical issues, which are inherent to the mode of operation of SEM (stability of electron beam, image drift, specimen charging, image distortion, dwell time), and by challenging requirements on contrast patterning at the specimen surface, which has to be compromised by the user. Sutton et al.[12] studied the image errors in SEM for different SEM systems. It was confirmed that image errors are a generic feature of SEM as image shifts occur at random positions during the image scanning process.[46] However, the effect of image drift on displacement calculations can be minimized by

image integration procedures without increasing overall scan time. In addition, Kammers et al.[27,81] and Di Gioacchino et al.[82] showed for SEM with a tungsten cathode that the noise of SEM images can be reduced by 1) large spot size or beam current, 2) a longer dwell time, and 3) multiple image integrations. This holds also for field-emission SEM (FESEM), as the overall noise of an FE cathode is already smaller than that for tungsten cathode.[82] Both the secondary electron (SE) and backscattered electron (BSE) contrast provide high-resolution micrographs with grayscale information. However, the sole application of the SE contrast is limited due to its high sensitivity for surface topography, leading to pronounced changes in grayscale contrast and outshining of some regions (e.g., surface steps, crack edges, etc.) during deformation. As the BSE contrast is very sensitive to orientation changes, its sole application is limited as well. Thus, an additional, randomly distributed, high-contrast pattern on the specimen surface is needed for good correlation results using SEM micrographs. Methods, which were tested in the past for high-quality and high-resolution DIC results, are microlithography,[83] the etching method,[10] or the application of colloidal, fine-dispersed, nanosized particles[15,84–86] onto the specimen surface. Kammers and Daly[87] described different patterning techniques applied for SEM–DIC such as FIB technique, nanoparticle patterning, or electron beam lithography accounting for both advantages and drawbacks of the different techniques.

3. DIC in MSE

Since the invention of DIC in 1983 by Sutton et al.,[40] this method has been subjected to large development and improvement regarding, in particular, the correlation algorithms and subpixel accuracy,[57] which is still an ongoing process, cf. H-DIC.[60,61] In the past 40 years, numerous publications on DIC in the field of MSE occurred.

To give an impression on the large variety of DIC applications in the last 20 years, Table S1, Supporting Information, shows a chronological overview of DIC in combination with OM and SEM but also with AFM, FIB technology, and CT. DIC in combination with AFM and FIB is mainly used for analysis of elastic properties of MEMS and residual stresses, respectively. It turned out that majority of DIC investigations were conducted in the field of plasticity, but they is also applied in the fields of fatigue and fracture mechanics. Finally, DIC serves for modeling and parameter identification (e.g., ref. [33]). The chronological overview starts in 2000 and includes scientific publications until 2020. However, it is impossible to issue a guarantee for completeness of these data.

In the following paragraphs, two major parts of DIC applications—DIC with OM and DIC with SEM—will be regarded in more detail.

3.1. DIC and OM

However at the end of the 1980s and in the 1990s, a majority of publications were related to the development and improvement of the method, and the number of publications using DIC for materials research increased rapidly in the 21st century. The DIC in combination with OM was applied in manifold research fields spanning from plasticity over fatigue and fracture mechanics to modeling. However, in the following section, only few of the numerous publications will be highlighted for different research fields. Although the resolution of DIC together with OM was limited to the grain scale, significant improvement was achieved in the past years due to the application of multiscale image techniques and the resolution was shifted to subgrain scale.

Plasticity. In the field of plasticity, DIC was applied in combination with OM under different loading conditions such as tensile or compressive loading, at different temperatures, and on various kinds of materials like aluminum, copper, titanium, various types of steels, and shape memory alloys, most of them in coarse-grained conditions. One of the first publications in the beginning of the 2000s was by Raabe et al.[88] and Sachtleber et al.[89] In these studies, 3D plastic displacement fields were investigated on coarse-grained polycrystalline aluminum during compression tests using the photogrammetry method. The photogrammetry method is comparable with DIC and was developed in the mid-1970s. Digital stereo pair images of the speckle pattern on the specimen surface were acquired using two high-resolution CCD cameras to measure the 3D surface coordinates of the specimen. In combination with grain orientation measurements by EBSD, strain localizations were identified at grain triple points and at grain boundaries aligned close to 45° to the compressive loading axis (LA). In addition, the experimental results were validated by CP finite element simulations.

Schroeter et al.[90] used the microgrid technique produced by photolithography to study large stretch and rotation fields during compressive and torsional loading of coarse-grained oxygen-free, high-conductivity (OFHC) copper (grain size: 70 μm) on a subgrain scale. It was shown that photolithography allows grid resolutions on the micrometer scale, resulting in measurements of intragranular deformation gradients in polycrystals with reasonable grain sizes. Moreover, the grid-line method was identified as a robust method to measure in-plane displacements on heavily deformed specimens over wide fields of view.

Zhang and Tong[91] conducted tensile tests on a binary coarse-grained Al-0.5 wt.%–Mg alloy in combination with optical records of the ink-decorated surface of the entire gauge length using a digital video CCD camera under white light illumination. Local plastic deformation fields and in-plane rigid-body rotations were obtained and correlated with a detailed Schmid factor and slip-system analysis and CP finite element simulations.

Fonseca et al.[92] described the technique of DIC in detail together with important experimental aspects as well as potential and shortcomings at that time. Furthermore, two case studies were presented—antler bone and ferritic steel—illustrating the wide field of applications in materials science ranging from biomedicine to materials engineering, "opening up a new quantitative front in in situ microscopy".[92]

Serrated plastic flow caused by dynamic strain aging such as PLC effect was studied by Zdunek et al.[93] using DIC on an aluminum alloy AA5182 with a grain size of 30 μm. The serrated plastic flow was correlated with the initiation of bands of strain localizations. Quite recently, Eskandari et al.[94] described the application of DIC using a speckle pattern in combination with macroscopic tensile tests at different temperatures (from room temperature [RT] up to 400 °C) and different strain rates on a

TWIP steel for studying serrated plastic flow as well. Strain localizations within individual bands were correlated with stress-assisted formation of ε-martensite and strain-induced α'-martensite at RT up to 180 ° and with twinning up to 400 °C.

Chow et al.[95] proposed a method for evaluation of total and elastic strains at the grain scale in a coarse-grained aluminum specimen under tensile loading by combination of in situ X-ray diffraction (XRD) (elastic strain) and DIC (total strain) measurements. Heterogeneities were found for both total and elastic strain values within individual grains, and locations of these heterogeneities were not necessarily identical.

Fatigue and fracture mechanics. In this research field, investigations using DIC based on optical micrographs were conducted to study the fatigue damage in terms of crack initiation and crack propagation including investigations on the size of the plastic zone in front of a crack tip. Bartali et al.[96,97] studied the micromechanisms of fatigue damage occurring in duplex stainless steel during low-cycle fatigue (LCF). The DIC calculations were conducted based on optical images of the specimen surface after electrochemical etching. Strain heterogeneities were detected on the grain scale and intense strain localizations were correlated with slip markings appearing on the specimen surface.

The work of Niendorf et al.[98] seems to be the first one where DIC measurements were carried out on ultrafine-grained materials using a Keyence digital microscope.

Sangid et al.[43] studied the fatigue crack growth and the evolution of the plastic zone in front of a crack tip both in nanocrystalline Ni–Co alloys and in poly- and single-crystalline AISI 316L steel specimens. In all cases, it was shown that DIC allowed for precise measurements of the displacement and strain fields during fatigue crack growth.

Mao et al.[99] conducted high-temperature (up to 1600 °C) DIC on C/SiC composite material during bending tests using single-edge-notched bending specimen (SENB) specimen geometry. For these investigations, a special high-temperature-resistant speckle pattern was developed consisting of a mixture of a high-temperature-resistant glue and ZrO_2 powder with particle sizes of about 10–20 nm, which was sprayed on the specimen surface using a high-pressure air brush gun.

In 2009, the first idea of fully coupled full-field measurements by combining DIC and IR-TG during fatigue experiments was established by Chrysochoos et al.[100] The deformation energy and the mean dissipated energy were estimated per cycle during fatigue of a DP steel DP 600 using the kinematic and thermal data recorded simultaneously by a two-camera setup on two opposite faces of a flat specimen. It turned out from these investigations that the mean deformation energy per cycle is homogeneously distributed, whereas a localization of dissipation energy is present already from the early start of the fatigue experiments.

Ahadi and Sun[51] used a two-camera setup on opposite sides of a compact tension specimen for fully coupled full-field measurements of displacement and temperature fields on a superelastic NiTi alloy with different grain sizes varying from 10 nm up to 1500 nm. Both in situ measurements showed continuous reduction in the size of the phase transformation zone at the crack-tip region with decreasing grain size. Moreover, the infrared measurements revealed regions of heating and cooling due to forward and reverse martensitic phase transformation (MPT) at the crack tip and the crack edges, respectively.

Modeling. As mentioned already in the introduction, the combination of DIC with numerical simulations is a very hot topic, in particular in the field of parameter identification. In particular, if spatial resolution of strain or stress heterogeneities at the scale of the existing microstructure is required, then so-called full-field computations using FEM have to be applied.[83] In contrast, for macroscopic mechanical response of polycrystalline material, either mean-field homogenization techniques or numerical simulations such as FEM were used, whereas homogenization models were applied for estimates on average response of the different phases including intraphase fluctuations.[83]

Besnard et al.[101] developed a new approach, which bridges experimental DIC measurements and numerical simulations. The approach is based on the application of so-called Q4–P1 kinematic functions known as FE simulation. However, it is not a real FE simulation, it uses only kinematical functions used in FE simulations for treatment of digital images in the sense of DIC for calculation of local strain fields. This approach was tested on aluminum alloy (AA5005) exhibiting PLC effect and revealed reasonably good spatial resolution also within localization bands, allowing, therefore, for space–time kinematic analysis of the PLC effect.

Héripré et al.[83] presented a methodology coupling experimental characterization of the microstructure, in situ and/or ex situ mechanical tests, and local strain field measurements with FE simulations. This linked methodology allows both for better understanding of the mechanical behavior of polycrystalline zirconium and titanium at the grain scale and for the identification of parameters of the crystallographic constitutive laws used for FE simulations. The Lueders band effect was studied by Avril et al.,[102] combining DIC measurements with the virtual field method (VFM) for the identification of elasto–visco plastic constitutive parameters.

Besides propagating strain localization phenomena, the plasticity of polycrystals and the resulting surface roughening including slip bands were also in the focus of coupled approaches such as those conducted by Zhao et al.[103] on oligocrystalline pure aluminum specimens, presenting a detailed comparison of CP finite element simulations and DIC results obtained during tensile deformation. The investigations showed that both the spatial arrangement of grain boundaries and the grain orientation have a significant influence on the origin of strain heterogeneity. Thus, strain localizations were promoted by the absence of dislocation barriers caused by grain boundaries, and inclined grain boundaries introduce additional shear strains, resulting in discrepancies with the crystal plasticity finite element method (CPFEM) simulations.

Saai et al.[104] presented a first approach on the combination of fully coupled full-field measurements of strain and temperature fields with micromechanical modeling of the global and local thermo–mechanical response on an aluminum bicrystal tested under tensile loading. The numerical results obtained by implementing dislocation-based constitutive laws of the single-crystal behavior FE code (ABAQUS Explicit) revealed, together with the experimental results, that the proposed model can predict heterogeneities in both strain and heat source fields caused by different grain orientations and grain interactions. Furthermore, it was

shown that variations of local strain and local heat source within grains are significantly higher in central parts of grains compared with grain boundaries.

Hosdez et al.[33] studied the evolution of a plastic zone in front of a crack tip using coupled elastic–plastic FEM simulations and experimental DIC measurements. The model approach was validated by a fatigue crack growth experiment on silicon and molybdenum-alloyed cast iron with spheroidal graphite. The coupled DIC-FEM approach uses the measured displacement fields as boundary conditions in elastic–plastic computations. The results of this coupled approach were compared with results applying the Irwin model for perfect plastic behavior under confined plasticity and plane stress condition. It turned out that no significant difference in terms of plastic zone size was found when applying either linear kinematic hardening or perfectly plastic behavior.

Improvement of resolution. While during the early 2000s the development of DIC technique and its applicability to various kinds of loading scenarios was in focus, in the beginning of the 2010s, the spatial resolution of DIC calculations became increasingly important. Thus, local strain measurements, which can be correlated with microstructural features, require a measurement technique with subgrain-level spatial resolution. Consequently, the subset size should be several times smaller than the grain size of the investigated material to guarantee a certain number of measuring points within an individual grain. Thus, grain size and magnification are the two main parameters for obtaining a large ratio of grain size to subset size.[105] There are two approaches to solve the problem of adequate spatial resolution: 1) using materials with large grain sizes observable at low magnification or 2) applying higher magnification. While the first approach has the benefit of larger optical depth of field, an easier speckle pattern creation, and easier alignment of strain fields with microstructure, most structural materials have smaller grain sizes of at least $<100\,\mu m$.[105] The realization of second approach of DIC on grain size level in combination with in situ testing at conventional load frames retrieves other difficulties such as vibrations, optical limitations, and speckle pattern quality. According to Carroll et al.,[105] the limitation of all in situ techniques is their restriction to a single FOV and with this to the observation of only a small number of grains. However, as DIC does not possess an inherent length scale, a technique allowing multiscale strain investigations using DIC measurements based on different optical magnifications was developed by different researchers. Thus, Carroll et al.[105] and Efstathiou et al.[45] applied a method of interrupted monitoring in combination with capture of multiple images of the FOV at the desired magnification, which were then stitched together before DIC calculations. Abuzaid et al.[106] used the same technique for the description of plastic strain localizations and fatigue microcrack formations in a nickel-base superalloy. **Figure 2** shows an example from Carroll et al.[105]

3.2. DIC and SEM

Similar to DIC in combination with OM, the application of DIC together with SEM has experienced rapid growth since 2000. On the one side, significant effort has been done for the evaluation of SEM inherent sources of errors and their handling and/or avoidance. On the other hand, significant efforts have been done also in the development of procedures for contrasting specimen surfaces for application of SEM–DIC. Different methods were developed and improved in the last years, starting from etching techniques over the application of grid technologies and lithography in the late 1990s up to deposition of nanoparticles and application of FIB technology. DIC in combination with SEM was applied in manifold research fields spanning from plasticity over fatigue and fracture mechanics up to modeling. However, in the following section, only few of the numerous publications will be highlighted for different research fields and a distinction will be done regarding the applied contrast technology. Although SEM–DIC is already well established since several years, significant progress was achieved with the aim of submicrometer resolution of local strain fields.

Natural pattern. In some cases, the natural surfaces of specimens can be used for DIC. Thus, materials after electrodeposition (e.g., ref. [107]), martensitic–ferritic and ferritic–pearlitic steels (e.g., ref. [108]), nickel-base superalloys (e.g., CMSX4[109]), or graphite cast iron,[110] provide sufficient surface pattern contrast suitable for DIC calculations with a resolution at least at the grain scale.

Etching. Besides the grid technique and the deposition of nanosized particles, the etching technique can be used as a much simpler technique, yielding good DIC calculation results. Tatschl et al.[10,111] used etching with a Fe(III)-chloride/hydrochloric acid solution on OFHC, resulting in fine micropits on the specimen surface. The studies on in situ tensile tests revealed strong

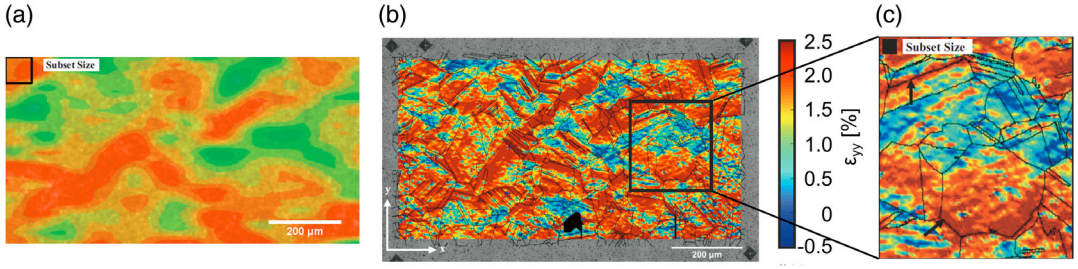

Figure 2. Results of DIC in combination with optical images. a) Low-resolution DIC—strain field ε_{yy} obtained on a single image of the whole AOI taken at low magnification (5×). b) High-resolution DIC—strain field of ε_{yy} with an overlaid grain boundary structure of the same AOI shown in (a). However, here the reference images and images of deformed states are stitched of 316 individual images of 31× magnification taken ex situ. c) Marked area in (b) with an indicated subset size. Note that the subset size in (c) is significantly smaller (14 µm) than the one used in (a) (89 µm), which results in higher resolution with subgrain-level accuracy. Reproduced with permission.[105] Copyright 2010, Elsevier.

heterogeneities of in-plane strain and local lattice rotations within individual grains.

Etching with 2% Nital agent was used by Kang et al.[112] for DIC on martensitic–ferritic steel in two different annealing states, revealing different strain distributions in both phases. Thus, it turned out that martensite starts to deform earlier in the tempered condition compared with the intercritical-annealed condition, where martensite does not deform until necking occurs. Moreover, local strains for crack initiation are higher in the tempered condition compared with the intercritical-annealed one. A similar procedure was applied by Ghadbeigi et al.[113] also on a DP steel. It was shown that the strain distribution is heterogeneous within the microstructure. Deformation bands developed with an inclination angle of 45 ° with significantly increased local strain values compared with the applied strain. High strain localizations were found also at interphase boundaries of martensite/ferrite.

While the resolution of the previous studies applying etching technique is more or less restricted to grain scale, Stinville et al.[114] showed, for a nickel-base superalloy (René 88 DT) after chemical etching, a resolution of DIC calculations in the micrometer range. The chemical–mechanical polishing process for 12 h resulted in fine secondary and tertiary γ′ precipitates with dimensions from 10 nm up to 200 nm. Based on the subgrain microstructure speckle pattern, strain heterogeneities can be captured at the micrometer scale. Using this chemical–mechanical etching process, Stinville et al.[115] conducted fatigue tests on the nickel-base superalloy in combination with a rather new method for DIC—the so-called H-DIC[60] (see section 2.2). It was shown for this new method that the resolution of DIC calculations is so high that it is possible to measure slip reversibility/irreversibility and slip accumulation during LCF loading. **Figure 3** shows impressively the high resolution of the local strain fields determined using the H-DIC approach separated in the tensile half cycle (Figure 3a) and the compressive half cycle (Figure 3c), resulting, finally, in the recoverable slip after the first complete cycle (Figure 3d).

Stinville et al.[116] proposed even a new method based also on the H-DIC for time-resolved DIC. With this method, it is possible to capture the evolution of both strain fields and strain localizations during deformation at the time scale from seconds to hours.

Electron lithography/grid technology. Efstathiou et al.[45] gave a short overview on the evolution and application of both techniques from the end of the 1990s to 2010. Thus, electron lithography/grid technology was applied in combination with SEM imaging on different types of materials varying from steel (e.g., refs. [117-120]) over copper and iron single crystals[80,121] and polycrystals,[90] respectively, to zirconium and titanium aluminides.[83] Thus, Amar et al.[67] introduced a special microgrid technology developed for in situ testing SEM in combination with local strain field measurements using DIC. The microgrid was created on the specimen surface by electron beam lithography. The width of the grid lines was about 0.25 μm and the distance between grid lines was about ten times the line width. Bugat et al.[120] applied a gold grid vacuum deposited by micro-electrolithography technique with a grid step size of 38 μm for investigations on crack initiation in a duplex stainless steel.

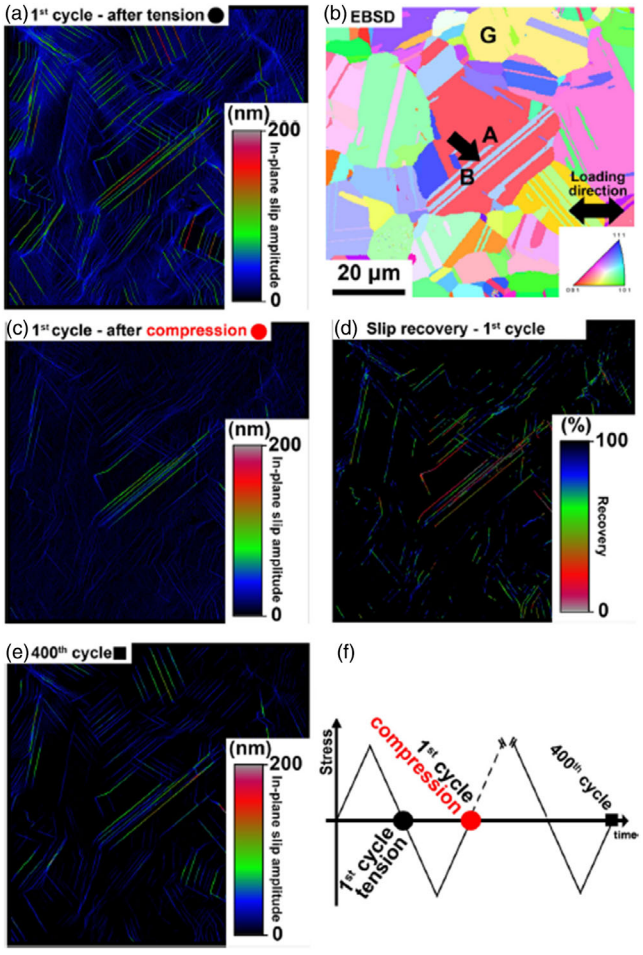

Figure 3. Slip localization during LCF loading of René88DT at a maximum applied stress of 1140 MPa during the first cycle after a) tension and c) compression as shown in (f) and after e) 400 cycles. HR-DIC measurements were carried out ex situ after unloading the specimen. a,c,d) The amplitude of the in-plane slip that describes the local displacement/step at the surface of the specimen induced by slip. b) Inverse pole figure (IPF) map of the associated microstructure given by EBSD measurements. d) Percentage of the slip irreversibility, which presents for each single slip band the amount of local in-plane displacement/step that is not recovered during the first cycle between the tensile and compressive loading. The slip irreversibility is calculated from the difference between the value of the amplitude of the in-plane slip after tensile and compressive load during the first cycle. This difference is normalized according the value of the in-plane slip after tensile load of the first cycle. Reproduced with permission.[115] Copyright 2019, Elsevier.

Crostack et al.[122] used photolithography and electron beam lithography to produce gratings of gold dots with dimensions of 5 and 1.5 μm for the first method and 0.5 μm for the latter method on the surface of metal–matrix composites (Ag/Ni and Al/Al_2O_3). In addition, the experimental investigations were corroborated by FE simulations. Strain localizations were found to occur in the ductile matrix in terms of narrow bands with an inclination angle of 45° with respect to the LA. A good agreement between experiments and FE simulations was found as well.

The microgrid technology was further improved by Biery et al.[66] using gold deposition on a glued nickel grid at the

specimen surface for in situ SEM investigations, which is much faster and less expensive than electron beam lithography. The authors[66] tested differences between grids well aligned with the scanning direction of the electron beam and nonaligned grids. It was shown that the best resolution is obtained when the boundaries of the grid markers are aligned by 45° with respect to the scanning direction.

Heripré et al.[83] introduced multiscale coupling of experimentally determined microstructural parameters such as morphology and texture and mechanical strain field analysis with finite element simulations. Morphology and textures of grains of zirconium and titanium aluminide polycrystals were evaluated from EBSD measurements. Microlithography was used for the application of a gold grid with a grid step size of 2 μm and a grid width of 300 nm. The investigations address both the macroscopic and the grain scale. In addition, possible sources of error of the measurements and several issues in the simulation regarding mesh refinement and boundary conditions were discussed.

Walley et al.[65] used the electron beam lithography for producing both a grid pattern and hafnium oxide speckle pattern at the surface of the nickel-base superalloy [René 104]. The used grid step size was 10 μm and electron lithography resulted in randomly distributed square-shaped hafnium oxide speckles with dimensions from 0.45 up to 0.7 μm. This kind of speckle pattern was successfully applied to in situ SEM creep tests at temperatures of >700 °C. However, it was also demonstrated that the square-shaped speckle pattern yields some limitations regarding the spatial resolution of DIC calculations.

Marteau et al.[123] used a gold microgrid with grid step sizes of 1 and 2 μm and bar widths of the grid in the range from 250 up to 50 nm for SEM–DIC calculations on ferritic and ferritic–martensitic steels. It turned out that in all investigated materials, occurring strain heterogeneities seem to be independent of the grain orientation, shape, or size but are significantly influenced by the surrounding grain. Strain partitioning between ferrite and martensite in DP steels was investigated also by Han et al.[124] Instead of microelectron beam lithography, the FIB technique was used for producing a microgrid with a grid step size close to 1 μm in a grid area of $40 \times 40\ \mu m^2$. It was observed that strain partitioning seems not to occur preferentially at ferrite–martensite interfaces. Furthermore, it turned out that independent on the orientation of the ferrite, the local morphology of the surrounding microstructure at ferrite–martensite interfaces seems to be responsible for high strain localizations.

However, although a high accuracy of strain measurements can be guaranteed by the application of a grid pattern on the specimen surface, the distance between grid lines or other markers restricts the resolution of strain measurements.[66] Therefore, techniques come into focus for contrasting specimen surface for high-resolution SEM–DIC.

Nanoparticle technology. The application of nanoparticles allows for a significant improvement of the resolution of SEM–DIC. Thus, different procedures of particle deposition use different types of particles ranging from precious metals (gold, silver, platinum, palladium) over "classical" metals (e.g., chromium, copper) to ceramic materials (e.g., SiO_2). Some applications of nanoparticles for studying phenomena of plasticity with micrometer resolution are reviewed in the following paragraphs.

Li et al.[125] used a method described by Scrivens et al.[63] for deposition of gold particle diameters in the range from 100 to 150 nm for both distortion correction and calibration of SEM imaging and validation of thermal experiments in SEM. Thus, the gold nanoparticles allowed during heating experiments on aluminum specimens in the range between 30 and 125 °C a standard deviation of 150×10^{-6} for strain measurements.

Pt nanoparticles deposited by the laser ablation process known as TTFA were used by Tschopp et al.[64] during in situ tensile tests on René 88DT in combination with SEM–DIC and EBSD. A correlation of maximum shear strain values with microstructure-related parameters such as the Schmid factor or distance from the grain boundary was found. Thus, increased maximum shear strain values were found with concurrently high Schmid factors close to grain boundaries or triple-junction points.

Joo et al.[126] used Ag nanodots of different dimensions for SEM–DIC on a DP steel. For the formation of nanodots, thin Ag films with thicknesses of 25, 50, 75, and 150 Å were grown on the steel specimen surface, which were then annealed at 300 °C for 5 min in vacuum. The sizes of the obtained nanodots were 23, 53, 95, and 189 nm, respectively, and the average spacings between individual nanodots were 20, 46, 70, and 135 nm, respectively. The Ag nanodots allowed for the quantitative analysis of strain localization even in small martensite islands with average sizes of 1–3 μm.

Submicron resolution of SEM–DIC measurements was obtained by Gioachinno et al.[82] using a gold speckle pattern on the surface of AISI 304 steel specimen. The gold speckles were obtained by an accelerated remodeling process of a thin gold layer resulting in gold nanodots in dimensions and spacings from about 30 up to 150 nm. It was shown that it was possible to observe strain localizations related with slip bands within austenitic grains with average grain size of 100 μm. Gioachinno et al.[85] even improved this technique to high-resolution DIC (HR-DIC), where it was possible to study the development of plastic strain at the microstructural scale and link it to the development of lattice curvature. Two different mechanisms were introduced, leading to lattice curvature caused by gradients of shear strains within slip bands approaching grain boundaries: 1) attenuation of slip within the primary SS and/or 2) activation of secondary SS in the vicinity of a grain boundary.

Kammers et al.[81] introduced a self-assembled citrate-stabilized gold nanoparticle surface-patterning technique producing from 15 nm-sized up to 136 nm-sized gold nanoparticles, enabling HR-DIC with 4 nm/pixel. The Au nanoparticles were tested in combination with two organosilane solutions, which are responsible for the self-assembling of the Au nanoparticles on the specimen surface. The Au nanoparticles were tested for HR-DIC during tensile tests on different materials such as pure aluminum, an aluminum alloy AA1100, nickel–chromium superalloy, and silicon carbide with comparable success. However, although a resolution of 4 nm/pixel was achieved, the slip bands revealed by Gioachinno et al.[82,85] in steel AISI 304 are sharper and straighter.

Kimiecik et al.[127] used also the self-assembled Au nanoparticles obtained by the method introduced by Kammers et al.[81] for studies on local strain fields in a superelastic NiTi shape memory alloy with an average grain size in the range from

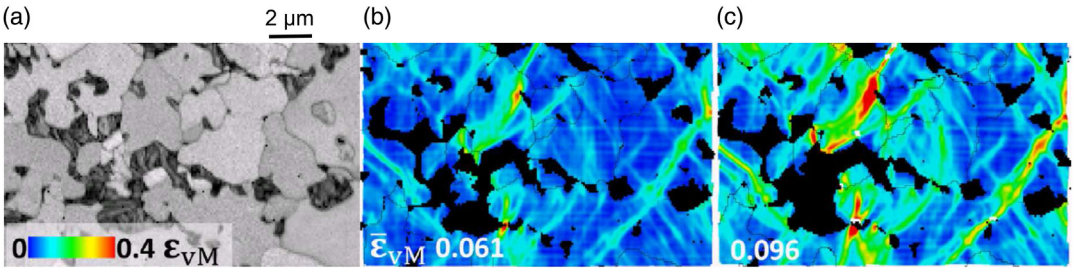

Figure 4. High-resolution SEM–DIC on DP steel DP800 at two different average equivalent Von Mises strains. a) Band contrast (BC) map of EBSD measurement. b) $\varepsilon_{vM} = 0.061$. c) $\varepsilon_{vM} = 0.096$. Reproduced with permission.[84] Copyright 2014, Elsevier.

3.5 up to 5 µm. The strain accommodation due to the thermoelastic MPT was highly heterogeneous. Moreover, for the martensitic band strain localization, up to 20% strain was detected, whereas for the austenitic regions, the strain remained as low as 1%.

Tasan et al.[84] used SiO_2 nanoparticles with dimensions of 11 nm in combination with SE imaging using an in-lens detector during the in situ biaxial tensile tests of two different DP steels with average grain sizes of the ferrite of 8.5 and 5 µm and 2.7 and 1.7 µm, respectively, for martensitic grains. **Figure 4** shows local strain fields with a resolution of DIC at the micrometer scale.

Tasan et al.[30] demonstrated the example of a DP steel where a coupled experimental–numerical methodology can be used to strengthen the understanding of the microstructure and mechanical properties of this alloy. The DP steel was used as model material for stress and strain partitioning as the two phases with comparable volume fractions—martensite and ferrite—experience different mechanical behaviors during mechanical loading. This integrated method combines the experimental investigations on the evolution of the deformed microstructure by EBSD and the evolution of strain localizations by DIC with the 2D full-field CP simulations. The model used for simulation was designed directly form microstructural data obtained from EBSD measurements, and the properties of the individual phases were obtained by additional inverse CP simulations of nanoindentation experiments on the initial microstructure. A good agreement between the results obtained from experimental investigations and simulations was achieved. However, the occurring discrepancies were related to known limitations in the experimental (3D effects) and numerical (damage and strain-gradient effects) methodologies.

Lim et al.[128] used CP simulations in combination with experimental results obtained on tensile-deformed oligocrystalline tantalum. The experiments were conducted with three aims: 1) measurement of the occurring grain rotation using EBSD, 2) measurement of the evolution of local strain fields using DIC, and 3) measurements of the surface profile with respect to out-of-plane distortions using an optical profilometer. The model used for CP simulations was carefully replicated from the initially measured microstructure. A reasonably good agreement between experimental observations (both in plane and out of plane) and model predictions with respect to the evolution of heterogeneous strain fields on the subgrain scale was achieved. Furthermore, it was shown that simple Schmid analysis seems not to be sufficient for predicting strain fields due to the influence of neighboring grains.

Jiang et al.[72] applied coupled HR-DIC and HR-EBSD on a single-crystalline nickel-base superalloy during in situ bending tests. The aim of these studies was to explore the mechanical behavior of the nearly [111] oriented single crystal and unravel the contributions of elastic deformation gradients and slip and rigid-body rotations to the entire deformation gradient. Opposite specimen surfaces were prepared either for HR-EBSD or for HR-DIC. For HR-DIC, polishing suspensions containing 250 nm-sized SiO_2 particles were shaken in an ultrasonic bath to obtain an even distribution of colloidal SiO_2 particles. They were then put on the ROI and, finally, dried on a hot plate at 150 °C for 5 min. Tests were done in the manner of interrupted monitoring. After each loading step of $\Delta F = 100$ N passing the yield strength, the AOI was imaged in SEM using an in-lens SE detector for DIC and the other surface was analyzed by HR-EBSD using two different SEM devices, respectively. Finally, it turned out that with the proposed method localized measurements of both the total deformation (HR-DIC) and the elastic deformation (HR-EBSD) were achieved. The link between both total and elastic deformation is bridged by the continuum or plastic deformation occurring on either side of the slip bands.[70]

Guan et al.[129] applied coupled CP modeling and HR-DIC single- and oligocrystalline nickel-base superalloys (CMSX4, MAR002) during cyclic loading using three-point bending experiments. SiO_2 particles with dimensions from 50 to 250 nm were used on one side of the specimen for HR-DIC, whereas the rare ones are used for HR-EBSD measurements. A significantly heterogeneous slip activation and plastic deformation have been found both in single crystals and in oligocrystals. However, a correlation between the addressed slip heterogeneities and strain localizations in both material states and the crack nucleation was not successful.

4. Case Studies of High-Resolution SEM–DIC

4.1. High-Alloy-Cast TRIP/TWIP Steels

For several decades, high-alloy TRIP and TWIP steels are, due to their exceptional mechanical properties, in the focus of scientific researches and industrial applications. While the TRIP effect with high work-hardening rates at concurrently excellent ductility (e.g., ref. [130]) is caused by MPT (e.g., ref. [131]), the TWIP effect caused by strain-induced twinning (e.g., ref. [132]) results in lower work hardening at even more pronounced ductility (e.g., ref. [133]). Recently, low-carbon, high-alloy CrMnNi-cast TRIP/

Table 2. Nominal chemical compositions and characteristic properties of the investigated CrMnNi TRIP/TWIP steels including relevant deformation mechanisms.

	Nominal chemical composition (wt %)							Characteristic properties		
	C	N	Cr	Mn	Ni	Si	Al	M_s[K]	SFE [mJ m^{-2}]	Deformation mechanisms
1	≤0.05	≤0.05	16	7	3	≤1	≤0.8	333	9	Formation of ε-martensite and α′-martensite
2	≤0.05	≤0.05	16	7	6	≤1	≤0.8	243	17	Formation of ε-martensite, α′-martensite, and SF-mediated twinning
3	≤0.05	≤0.05	16	7	9	≤1	≤0.8	233	25	Movement of regular dislocations and SF-mediated twinning

TWIP steels were developed by Weiss et al.[134] based on a chemical design concept enabling both TRIP and TWIP effect depending on the chemical composition and the application temperature. The CrMnNi steels (0.05 wt% C, 0.05 wt% N, 16 wt% Cr, and 7 wt% Mn) with varying Ni content (3 wt % ≤ c_{Ni} ≤ 9 wt%) were intensively studied in coarse-grained, as-cast, as well as fine-grained powder metallurgical states under different loading conditions.[135–139] The microstructural processes behind the outstanding mechanical properties such as dislocation glide, strain-induced twinning, and MPT (e.g., ref. [140]) as well as their kinetics are quite well understood (e.g., refs. [141–145]). Both the chemical composition and the deformation temperature influence the TRIP and TWIP effect,[146] as they have a significant influence on austenite stability as well as on SFE. The austenite stability can be expressed by the martensitic start temperature M_s, which can be calculated from the chemical composition according to the approach of Jahn et al.[147] The SFE energy was determined experimentally by Rafaja et al.[148,149] by in situ XRD during three-point bending experiments. In general, the lower the nickel content, the lower the austenite stability and the SFE at the given chemical composition with respect to carbon, nitrogen, chromium, and manganese. Thus, MPT is the predominant mechanism[140] at low austenite stability and low SFE, respectively, whereas strain-induced twinning dominates in steels with higher austenite stability and SFE. **Table 2** shows the chemical compositions as well as characteristic properties of several batches of as-cast specimens describing the austenite stability and dominating deformation mechanisms.

4.2. Deformation Mechanisms and Microscopic Strain Localizations

Detailed microstructural investigations revealed that the MPT occurs in deformation bands. The structure of these bands—called ε-martensite in the literature[150]—is indexed as hexagonal lattice structure by EBSD as well as XRD experiments. However, the high density of stacking faults (SFs) within these bands yields a regular arrangement on, in average each second, {111} lattice plane, causing a stacking sequence of atomic layers of type ABAB, which is related to a hexagonal close-packed (hcp) lattice structure in contrast to ABCABC sequence of a face-centered cubic (fcc) crystal lattice in average over a larger volume.[148,151,152] In contrast, the ε-iron phase obtained at high hydrostatic pressures exhibits a real hexagonal lattice structure.[153] Therefore, it has to be distinguished between deformation-induced ε-martensite with a hexagonal structure formed inside deformation bands and pressure-induced hcp ε-iron phase.[153] Therefore, in the following paragraphs, the deformation bands with hexagonal structures were treated as highly distorted austenite due to the high density of SFs (compare[148,151,152]). MPT $\gamma \rightarrow \alpha'$ is, consequently, considered as a shear interaction of SFs on different slip planes (SP) in agreement with various studies.[154–156] The kinetics of these deformation mechanisms were analyzed in the past depending on the austenite stability (variation in the chemical composition) and the SFE (different deformation temperatures) using in situ acoustic emission (AE) measurements during quasistatic tensile loading.[141–145] It turned out that besides movement of partial dislocations forming either ε-martensite bands or twin bundles, the movement of regular dislocations has an important contribution to the strain-hardening behavior of these steels. Furthermore, it was shown that the importance of movement of regular dislocations increases with an increase in austenite stability and deformation temperature. Moreover, the formation of α′-martensite decreases with an increase in both austenite stability and SFE.

Finally, the resulting microstructure, in particular of TRIP steels, is very complex (see **Figure 5**) and consists of 1) deformed austenite containing regular and partial dislocations as well as SFs, 2) deformation bands, which contain a high density of largely extended SFs resulting either in ε-martensite (hcp) or twin configuration (fcc), and, finally, 3) α′-martensite grains inside the ε-martensite bands.

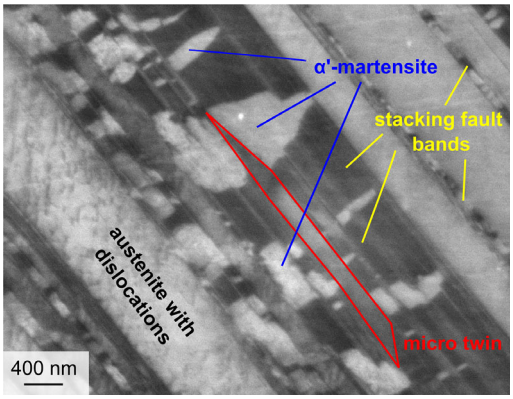

Figure 5. Microstructure of steel X5CrMnNi16-7-6 after quasistatic tensile loading at RT up to $\varepsilon = 15\%$ consisting of deformed austenite, deformation bands containing SFs resulting in ε-martensite (yellow) or microtwins (red) and α′-martensite (blue). Reproduced with permission.[168] Copyright 2015, Springer.

According to Brechet and Louchet,[5] the formation of deformation bands consisting of a high density of SFs can be understood as a static strain localization on the micrometer scale. Thus, the term "deformation band" is defined as a band-like region with deviating strain state in comparison with the surrounding material, which is often accompanied by variation in orientation and/or dislocation density. The term "deformation band" covers also regions with packages of fine strain-induced twins—so-called twin bundles or SF-mediated twins. Deformation bands are restricted to the grain size, as analogous to slip bands they are determined by the crystallographic nature of the material due to the occurring deformation mechanisms' dislocation glide or twinning. The strain localization in deformation bands is caused by pile-ups of regular dislocations or partial dislocations and is, consequently, influenced by grain size. Thus, the grain boundaries of a material act as barriers for dislocation motion leading to pile-ups. In addition, dislocation sources in the grain interior (e.g., Frank–Read sources) are active during plastic deformation. Consequently, a decrease in grain size will lead to so-called double-ended slip bands by pile-ups on two opposite grain boundaries. Therefore, stress concentrations arise at the grain boundaries, leading either to activation of parallel slip bands in close vicinity within the same grain or the slip transfer into neighboring grains.

An excellent method for the determination of local strain fields is DIC in combination with in situ deformation tests in high-resolution SEM. In the past, several investigations on low-carbon martensitic steels,[157] duplex steels,[84] DP steels,[113,158] or other materials (e.g., ref. [127]) have already demonstrated that local strain fields within deformation bands can be evaluated using this method with a resolution in the range of several micrometers. However, in case of metastable austenitic steels, the strain localization caused by the formation of deformation bands is accompanied by a second strain localization caused by MPT. The experimental evaluation of strain localization caused by individual α'-martensite grains is still an open question. Moreover, as both the thickness of these deformation bands and the size of the formed α'-martensite variants are in the range of few micrometers (see Figure 5) only, there is a strong request on the high-resolution DIC method to resolve the shear values and directions within individual α'-martensite islands.

In the following section, local strain fields and calculated magnitudes of shear obtained via high-resolution DIC in the submicrometer range—called μDIC—are presented. The term high-resolution is related to both the lateral resolution of DIC calculations and strain resolution.

4.3. High-Resolution μDIC on Cast TRIP/TWIP Steels

The high-resolution μDIC experiments were conducted on low-carbon, high-alloy metastable austenitic steels in as-cast conditions after solution annealing (1323 K, 30 min, N_2-gas quenching), showing TRIP/TWIP effect. The grain size of the as-cast microstructure covered a quite large range from 50 to 2000 μm. Miniaturized flat tensile specimens (total length: 50 mm) with a gauge length of 12 mm and a rectangular cross section of $4 \times 2.25\,mm^2$ were prepared by careful grinding and polishing up to 1 μm grade. Final preparation step was vibration polishing for 24 h (Bühler VibroMet) using colloidal SiO_2 suspension with 0.02 μm particle size followed by carefully water cleaning for 1 h.

In situ tensile deformation experiments were conducted via FESEM (MIRA3 XMU, TESCAN, Czech Republic) using a push–pull loading stage (Kammrath & Weiss, Germany), enabling maximum load range of ±10 kN. The tensile tests were conducted both at RT and at elevated temperatures (373 or 473 K), respectively. Heating was realized using a heating device, allowing for temperatures up to 1073 K. The loading stage was cooled using a water pipe system. The tests were interrupted at defined intervals of elongation ($\Delta l = 50\,\mu m$) up to a total strain of $\varepsilon = 15\%$. High-resolution SEM micrographs (2048×1536 pixels) using SE contrast were taken from a randomly chosen AOI. This results in a pixel resolution of 25 nm/pixel at 4000× magnification. Due to stress relaxation effects during interruption of tensile deformation after each loading step, a stress stabilization for 90 s was maintained before taking the micrographs to avoid drift distortions of the captured micrographs. A line iteration (20× line average) and a dwell time of $1\,\mu s\,pxl^{-1}$ were used to capture the micrographs, which resulted in nearly distortion-free micrographs with a capture time of 67 s per micrograph at the given image resolution.

As described previously, the essential prerequisite for successful DIC is a suitable contrast pattern at the surface of the investigated specimen. Among different possibilities creating contrast patterns at the specimen surface (SiO_2 particles, Pt nanoparticles), the well-known etching technique provided the best results of contrast patterning for high-resolution μDIC. Therefore, the surfaces of the specimens were carefully etched using the V2A etching agent (100 ml distilled water, 100 ml hydrochloric acid, 10 ml nitric acid, and 0.3 ml pickling inhibitor) for 1 min at 333 K. Applying this procedure, randomly distributed etch pits with dimensions less than 200 nm were obtained, giving high-contrast patterns recommended for good DIC correlation results.

The software ARAMIS (GOM, Germany)[73] was used for calculation of displacement fields using a reference field size of 30×30 pixels and a step size of ten pixels. Local strain fields were calculated from the displacement fields and were displayed in terms of the von Mises equivalent strain (ε_{vM}). In addition, different components of the strain tensor (ε_{xx}, ε_{xy}) and major and minor strains (ε_1, ε_2) were displayed, and magnitudes of shear were calculated along defined lattice directions.

After finishing the tensile tests at maximum elongation of $\varepsilon = 15\%$, the etched specimen surfaces were removed again by vibration polishing for 12 h or multiples of it. Finally, the microstructures of the AOIs were investigated using EBSD technique.

In the following, the results of the local strain field measurements will be discussed for three CrMnNi cast steels with different austenite stabilities (see Table 2) at two test temperatures each. First, the steel with the highest austenite stability will be discussed.

Steel X5CrMnNi16-7-9 at RT. **Figure 6** shows the evolution of the local strain fields within one individual austenitic grain during tensile loading at different global strain levels. The complete evolution over the entire loading path up to $\varepsilon = 15\%$ is shown in a video sequence provided in Supporting Information, S2. At an

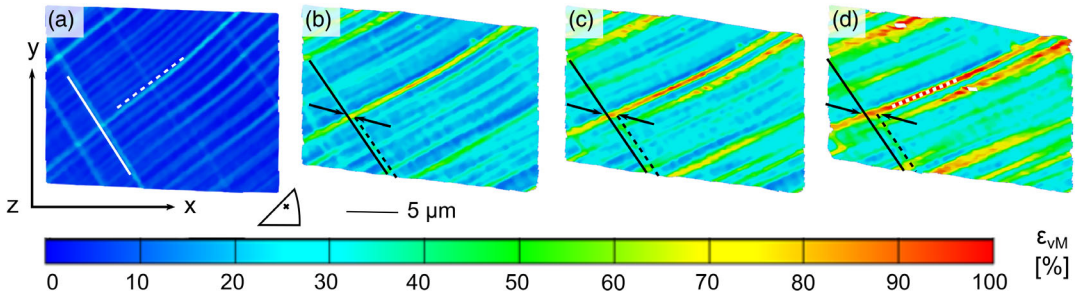

Figure 6. Local strain fields in terms of von Mises equivalent strain ε_{vM} for steel X5CrMnNi16-7-9 evolving during quasistatic tensile loading at RT. a) $\varepsilon = 1\%$, b) $\varepsilon = 2\%$. c) $\varepsilon = 5\%$, and d) $\varepsilon = 15\%$. LA is parallel to *x*-direction. Crystallographic orientation of austenitic grain is given in schematic stereographic standard triangle (SST). Adapted with permission.[141] Copyright 2020, Springer.

applied strain of about 1 % (see Figure 6a), deformation bands aligned along two SSs appear at different angles β related to the LA: $\beta_1 = 37°$ (dashed white line) and $\beta_2 = 122°$ (bold white line), respectively. The latter one ($\beta_2 = 122°$) belongs to the primary SS with the highest Schmid value ($\mu = 0.45$), whereas the former one ($\beta_1 = 37°$) is related to the secondary SS with a significantly lower Schmid value ($\mu = 0.36$). Only few bands of the primary SS have been developed, whereas the number of bands related to the secondary system is significantly higher. The strain is homogeneously localized inside the bands, whereas the austenitic matrix between the bands remains almost unstrained (see Figure 6a). Already at $\varepsilon = 1\%$, the equivalent strain ε_{vM} inside the bands is significantly increased ($\varepsilon_{vM} > 10$ %). The local strain values increase within these bands during further plastic deformation. In addition, at about $\varepsilon = 2\%$, a significant shear of the deformation bands arranged at 122° becomes apparent at the intersection point of both systems indicated by the bold and dashed black lines together with the two black arrows in Figure 6b. In some of the deformation bands belonging to the secondary system ($\beta_1 = 37°$), higher local strain values start to develop ($\varepsilon_{vM} > 50\%$). At $\varepsilon = 15\%$ (Figure 6d), the strain is more or less homogeneously distributed within the austenitic grain at $\varepsilon_{vM} \approx 30\%$, except for few bands with significantly higher strain values ($\varepsilon_{vM} > 70$ %).

Figure 7 shows the correlation of the bands with increased strain values (Figure 6d) with the developed microstructure (Figure 7b,c). It becomes apparent that these bands are related to twin bundles formed in the austenitic grain.

Twin boundaries, which are characterized by a misorientation angle/axis pair of 60°⟨111⟩, are highlighted in red color in Figure 7c. However, it is also visible that not all developed deformation bands have been indexed as twin configurations by EBSD. In addition, tiny twins have been formed also along the primary system, indicated by black arrows (Figure 7a–c), which were hardly resolved in the local strain field (Figure 7a).

Steel X5CrMnNi16-7-9 at 473 K. The increase in temperature results in a change in the ongoing deformation mechanisms. Thus, the ability to form Shockley partial dislocations contributing to twin formation decreases due to an increase in the SFE, $\Delta\gamma_{SF}$. Remy[159] reported an increase from about 0.05 up to 0.1 mJ m^{-2} for a temperature increase of $\Delta T = 1$ K. For the present case, this means that the SFE will increase for deformation at 473 K by 10 mJ m$^{-2} \leq \Delta\gamma_{SF} \leq$ 20 mJ m^{-2}. The principal deformation mechanisms for steel X5CrMnNi16-7-9 at 473 K will be, therefore, expected to be the movement of regular dislocations. This becomes apparent both from the evolution of local strain fields and from microstructural investigations. **Figure 8** shows the von Mises equivalent strain fields at $\varepsilon = 2\%$ (Figure 8a) and $\varepsilon = 15\%$ (Figure 8b). The formation of numerous slip bands along the primary SS with increased strain values becomes apparent from the beginning of the deformation process. With increasing applied strain, both the number of slip bands and the strain within the bands increase. Finally, the strain seems to be more or less homogenously distributed in the entire austenitic grain. The EBSD measurements at $\varepsilon = 15\%$ revealed a

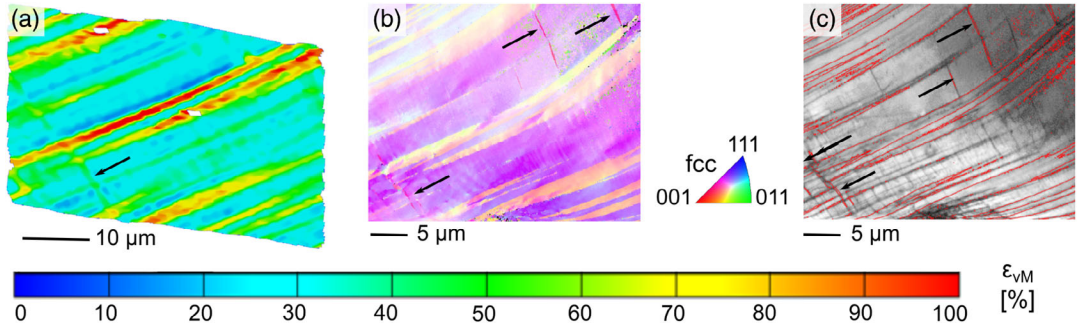

Figure 7. a) Local strain field ε_{vM} of steel X5CrMnNi16-7-9 obtained at $\varepsilon = 15\%$ at RT corroborated by results of EBSD measurements (b,c). b) Crystallographic orientation map of region (a) in IPF color code related to LA (horizontal). c) BC map with indicated twin boundaries (red lines). Adapted with permission.[141] Copyright 2020, Springer.

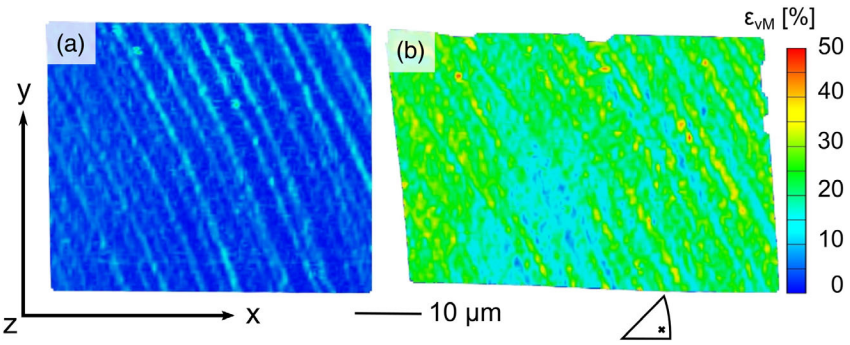

Figure 8. Local strain fields in terms of von Mises equivalent strain ε_{vM} for steel X5CrMnNi16-7-9 evolving during quasistatic tensile deformation at 473 K: a) $\varepsilon = 2\%$ and b) $\varepsilon = 15\%$. LA is parallel to *x*-direction. Crystallographic orientation of austenitic grain is given in schematic SST. Adapted with permission.[141] Copyright 2020, Springer.

fully austenitic microstructure without twin bundles. Thus, neither ε-martensite nor α'-martensite nor twins were formed at $T = 473$ K.

These findings agree well with studies on the kinetics of deformation mechanisms for this steel conducted by AE measurements both at RT[142] and at 373 K.[143] The AE results demonstrated that a change in the principal deformation mechanism for this steel occurs. Thus, at RT, both the formation of twins by partial dislocations and the movement of regular dislocations were identified as deformation mechanisms, whereby twin formation is the principal mechanism. At 373 K, the movement of regular dislocation was found to be the sole deformation mechanism.

Steel X5CrMnNi16-7-6 at RT. **Figure 9** shows the evolution of the local strain field within one individual austenitic grain during tensile loading at different global strain levels. The formation as well as the growth of deformation bands in thickness and number can be followed for the complete loading path up to $\varepsilon = 15\%$ both on the etched surface and in the local strain field images in the video provided in Supplementary Materials S3. At an applied strain of about 1%, already several deformation bands aligned along one activated SS can be recognized. The strain is localized inside the bands as it becomes evident from the displayed strain fields in Figure 9. However, the austenitic matrix between the deformation bands remains nearly unstrained, the strain inside the bands is significantly increased (>8%) already at 1% of applied strain. However, the strain is homogenously distributed within the bands.

The local strain inside these deformation bands increases with a further increase in global strain. At around $\varepsilon = 5\%$, additional areas with higher localized strain values were detected. With ongoing deformation, the number of such areas of higher local strain values increases as well.

Figure 10 shows the calculated local strain field at $\varepsilon = 15\%$ (Figure 10a) and results of EBSD measurements on this AOI showing the phase composition (Figure 10b) and the crystallographic orientation of the α'-martensite grains with respect to the LA (Figure 10c). It becomes obvious from EBSD measurements that the regions with homogenously localized strain correlate well with hexagonally indexed regions formed by the high density of SFs. The areas with highest local strain values were identified as α'-martensite that formed inside the deformation bands (compare Figure 10a,c). The narrowest deformation band detected by DIC (see white arrows in Figure 10a) had a thickness of about 500 nm, which was confirmed by the EBSD phase map. Thus, even strain localizations in bands with a thickness less than 1 µm were detected by this high-resolution DIC method based on the etched-pattern contrast at the specimen surface in combination with high-resolution SEM images in SE contrast, which is really worth to be emphasized as µDIC.[160]

Steel X5CrMnNi16-7-6 at 373 K. The steel X5CrMnNi16-7-6 undergoes a change in the occurring deformation mechanisms with an increase in temperature. However, at RT, the MPT from austenite via ε-martensite into α'-martensite occurs; at temperature $T \geq 313$ K, the deformation mode changes to the formation

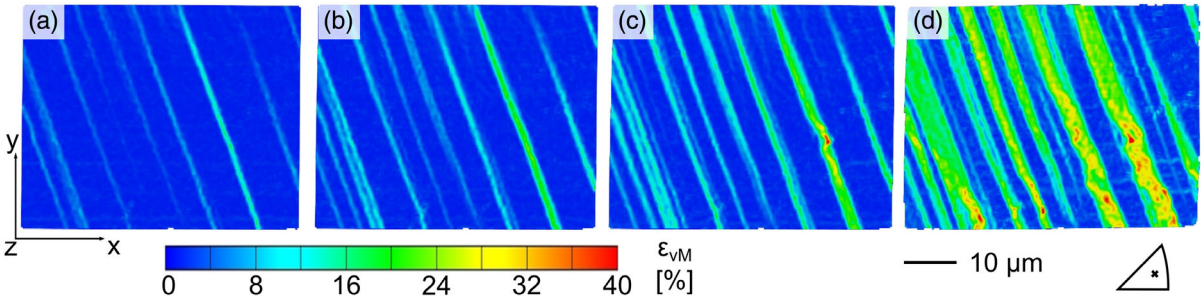

Figure 9. Local strain fields in terms of von Mises equivalent strain ε_{vM} for steel X5CrMnNi16-7-6 evolving during quasistatic tensile deformation at RT. a) $\varepsilon = 1\%$, b) $\varepsilon = 2\%$, c) $\varepsilon = 5\%$, and d) $\varepsilon = 15\%$. LA is parallel to *x*-direction. Crystallographic orientation of austenitic grain is given in schematic SST. Adapted with permission.[141] Copyright 2020, Springer.

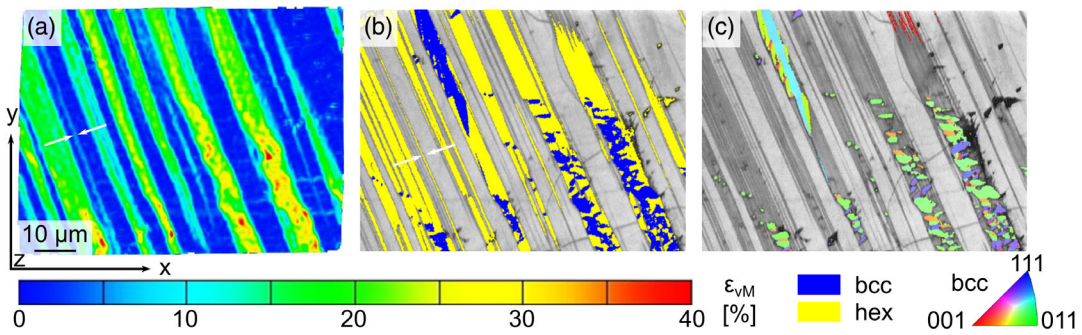

Figure 10. a) Local strain field ε_{vM} of steel X5CrMnNi16-7-6 obtained at $\varepsilon = 15\%$ at RT corroborated by results of EBSD measurements (b,c). b) BC map with superimposed phase map: gray: austenite; yellow: ε-martensite; blue: α'-martensite. c) BC map with superimposed crystallographic orientation map of α'-martensite of region (a) in IPF color code related to LA (horizontal). Adapted with permission.[141] Copyright 2020, Springer.

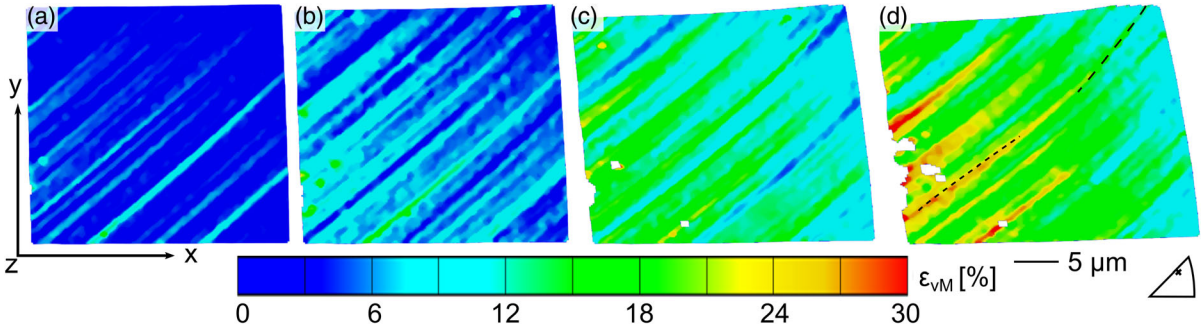

Figure 11. Local strain fields in terms of von Mises equivalent strain ε_{vM} for steel X5CrMnNi16-7-6 evolving during quasistatic tensile deformation at 373 K. a) $\varepsilon = 1\%$, b) $\varepsilon = 2\%$, c) $\varepsilon = 5\%$, and d) $\varepsilon = 15\%$. LA is parallel to *x*-direction. Crystallographic orientation of austenitic grain is given in schematic SST. Adapted with permission.[141] Copyright 2020, Springer.

of twin bundles (see ref. [141]). This effect is caused both by an increase in the SFE and by a decrease in the thermodynamic driving force for the strain-induced MPT. This change in the deformation mechanisms becomes apparent also from the evolution of local strain fields at 373 K. **Figure 11** shows the evolution of the local strain fields within one individual austenitic grain during tensile loading at different global strain levels. The formation, the growth of deformation bands in thickness and numbers, as well as the change in the alignment of the deformation bands with respect to the LA can be followed for the complete loading path up to $\varepsilon = 15\%$ both on the etched surface and in the local strain field images in a video provided in Supporting Information, S4. Comparable with the results obtained at RT, deformation bands start to develop early in the deformation process at around $\varepsilon = 1\%$ characterized by homogenous strain localizations at around $\varepsilon_{vM} > 6\%$ (Figure 11a). With an increase in applied strain, again the number of bands, their thickness, as well as the strain within some of these bands increase as well (Figure 11b-d). In addition, a pronounced curvature of the deformation bands at higher strain values is apparent, indicated by black dashed lines in Figure 11d.

Results of EBSD measurements conducted at $\varepsilon = 15\%$ at the AOI are shown in **Figure 12**. These measurements revealed that the majority of the developed deformation bands exhibits a twin

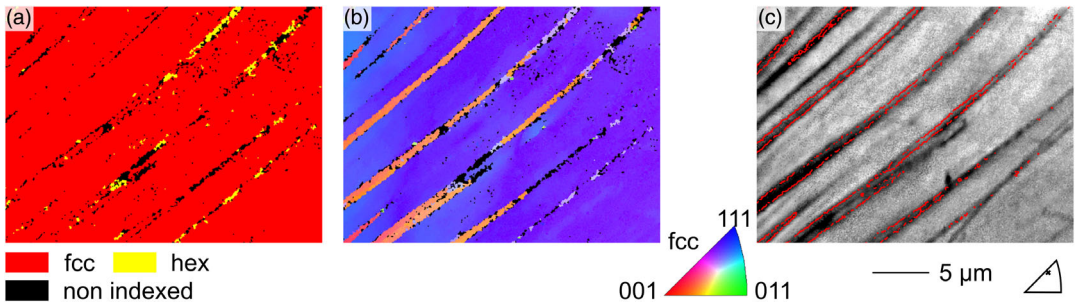

Figure 12. Results of EBSD measurements of steel X5CrMnNi16-7-6 obtained at $\varepsilon = 15\%$ at 373 K. a) Phase map: red, austenite; yellow, ε-martensite; black, nonindexed. b) Crystallographic orientation map of austenite and ε-martensite in IPF color code related to LA (horizontal). c) BC map with indicated twin boundaries (red lines). Adapted with permission.[141] Copyright 2020, Springer.

orientation to the austenitic matrix (Figure 12b,c). Minor part of these bands exhibits a hexagonal lattice structure (see yellow color in Figure 12a). Thus, both the formation of ε-martensite (hcp) and the formation twin bundles occurs at this deformation temperature. Moreover, these bands, which have transformed already to the twin configuration, are related to higher strain values $\varepsilon_{vM} > 20\%$.

These results agree well with investigations conducted by XRD,[161] TEM,[162] and AE measurements.[142] All these investigations showed, together with the mechanical properties under quasistatic loading in tension or compression at different temperatures,[159] that a transition from TRIP to TWIP effect occurs at temperatures $T \geq 313$ K.

Steel X5CrMnNi16-7-3 at RT and 373 K. This steel exhibits the lowest austenite stability and, therefore, the highest ability for MPT as the martensite start temperature is $M_s = 333$ K well above RT. Thus, this steel shows a strain-induced MPT both at RT and at 373 K but of course to a lower extent at the higher temperature. **Figure 13** and **14** show the local strain fields and results of EBSD measurements obtained at RT and 373 K, respectively. At both temperatures, the formation of deformation bands along two activated SSs occurs accompanied by strain localization within these bands (Figure 13a and 14a). Comparable with previously described steels, the number of bands, their thickness, as well as the localized strain values increase with an increase in applied strain (Figure 13b and 14b). The correlation with the microstructure reveals in both cases that the high strain values were caused by the formation of ε-martensite and α'-martensite.

However, the thickness of the deformation bands and, consequently, the size of the α'-martensite grains is significantly smaller compared with steel X5CrMnNi16-7-6. Therefore, a correlation of high strain values with individual α'-martensite variants, as shown in Figure 10b,c, is not possible. At $T = 373$ K, the formation of α'-martensite is less pronounced but still present resulting also in strain localizations.

4.4. Magnitude of Shear for α'-Martensite, ε-Martensite, and Twin Bundles

Strain localizations occurring in high-alloy TRIP/TWIP steels are caused both by the formation of deformation bands consisting of either ε-martensite (high density of SFs) or SF-mediated twin bundles and by the formation of strain-induced α'-martensite. Both intersection points of deformation bands on different SSs and intersection points of two individual SFs on different {111} planes are favored sites for the formation of α'-martensite.[150]

It is known from theoretical considerations[150,155,156] that the formation of ε-martensite takes place by shear on {111} planes along a ⟨112⟩ direction comparable with the twinning mechanism. While the magnitude of shear s for twins is known to be $s_{twin} = \sqrt{2}/2 = 0.707$, the magnitude of shear for ε-martensite is only half of the twinning shear

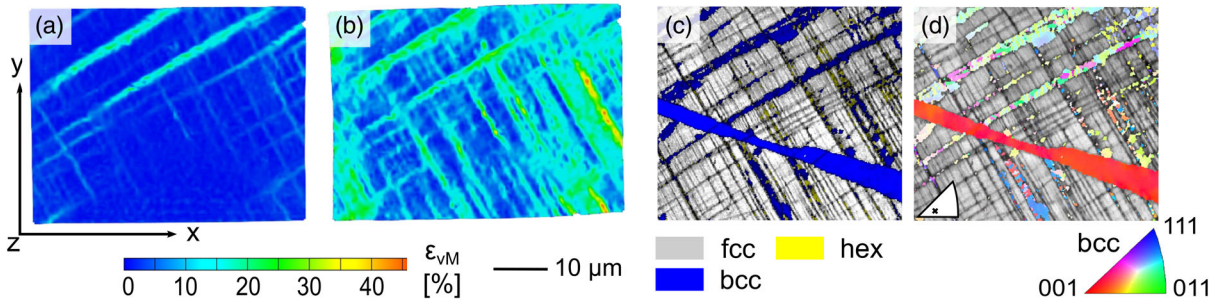

Figure 13. Local strain fields in terms of von Mises equivalent strain ε_{vM} (a,b) for steel X5CrMnNi16-7-3 evolving during quasistatic tensile deformation at RT together with results of EBSD measurements at $\varepsilon = 15\%$. a) $\varepsilon = 3\%$ and b) $\varepsilon = 15\%$. c) BC map with superimposed phase map: gray, austenite; yellow, ε-martensite; blue, α'-martensite. d) BC map with superimposed crystallographic orientation map of α'-martensite/δ-ferrite of region (b) in IPF color code related to LA. LA is parallel to *x*-direction. Crystallographic orientation of austenitic grain is given in schematic SST. Adapted with permission.[141] Copyright 2020, Springer.

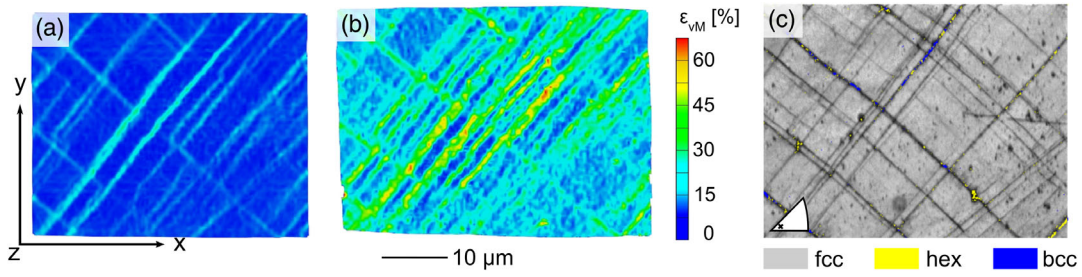

Figure 14. Local strain fields in terms of von Mises equivalent strain ε_{vM} (a,b) for steel X5CrMnNi16-7-3 evolving during quasistatic tensile deformation at 373 K together with (c) results of EBSD measurements at a) $\varepsilon = 12\%$, b) $\varepsilon = 3\%$, and c) $\varepsilon = 12\%$. BC map with the superimposed phase map: gray: austenite; yellow: ε-martensite; and blue: α'-martensite. LA is parallel to *x*-direction. The crystallographic orientation of austenitic grain is given in the schematic SST. Adapted with permission.[141] Copyright 2020, Springer.

$s_\varepsilon = \sqrt{2}/4 = 0.35$. Furthermore, it was shown by Schumann[155] that the interaction of two partial dislocations on two SPs of type {111} can yield double shear in the intersection area, which is beneficial for the formation of α'-martensite nucleus. Therefore, the formation of α'-martensite is energetically more favorable through the intermediate state of ε-martensite or SFs ($\gamma \rightarrow \varepsilon/\mathrm{SF} \rightarrow \alpha'$). Furthermore, Schumann[156] mentioned that not all shear directions in the activated SPs lead to beneficial shear and, thus, a variant selection of the formed α'-martensite is expected. The mechanisms of the formation of α'-martensite as well as the variant selection of α'-martensite were investigated by numerous authors (e.g., refs. [163,164]) even by MD simulations (e.g., refs. [165–167]). However, up to now, the magnitude of shear could not be determined experimentally, neither for the deformation bands with high density of SFs and nor for twin bundles or for α'-martensite. Thus, to prove the theoretical predictions, μDIC seems suitable to verify the magnitudes of shear.

The discussion of magnitude of shear for different microstructural constituents of the studied steels will start with the alloy X5CrMnNi16-7-6, which shows an intense formation of α'-martensite at RT and formation of SF-mediated twin bundles at 373 K. This will be followed by results on steel X5CrMnNi16-7-9, exhibiting formation of SF-mediated twins at RT.

X5CrMnNi16-7-6 at RT. The discussion is focused on the part of deformation bands, showing a high number of martensitic grains with different orientations (see lower right corner in Figure 10b,c). **Figure 15** shows the evolution of the normal strain ε_{xx}, the minor strain ε_2, the shear strain ε_{xy}, and the absolute value of the magnitude of shear $s_{[0\bar{1}1]}$ of the AOI at different applied strain values ($\varepsilon = 2\%$ (a), $\varepsilon = 4\%$ (b), $\varepsilon = 7\%$ (c), and $\varepsilon = 12\%$ (d)). In addition, the direction of the minor strain (Figure 15a–d, ε_{xx}, first row) and the direction of the major strain (Figure 15a–d, ε_2, second row) are indicated by small black arrows. The visualization of normal strain ε_{xx} reveals

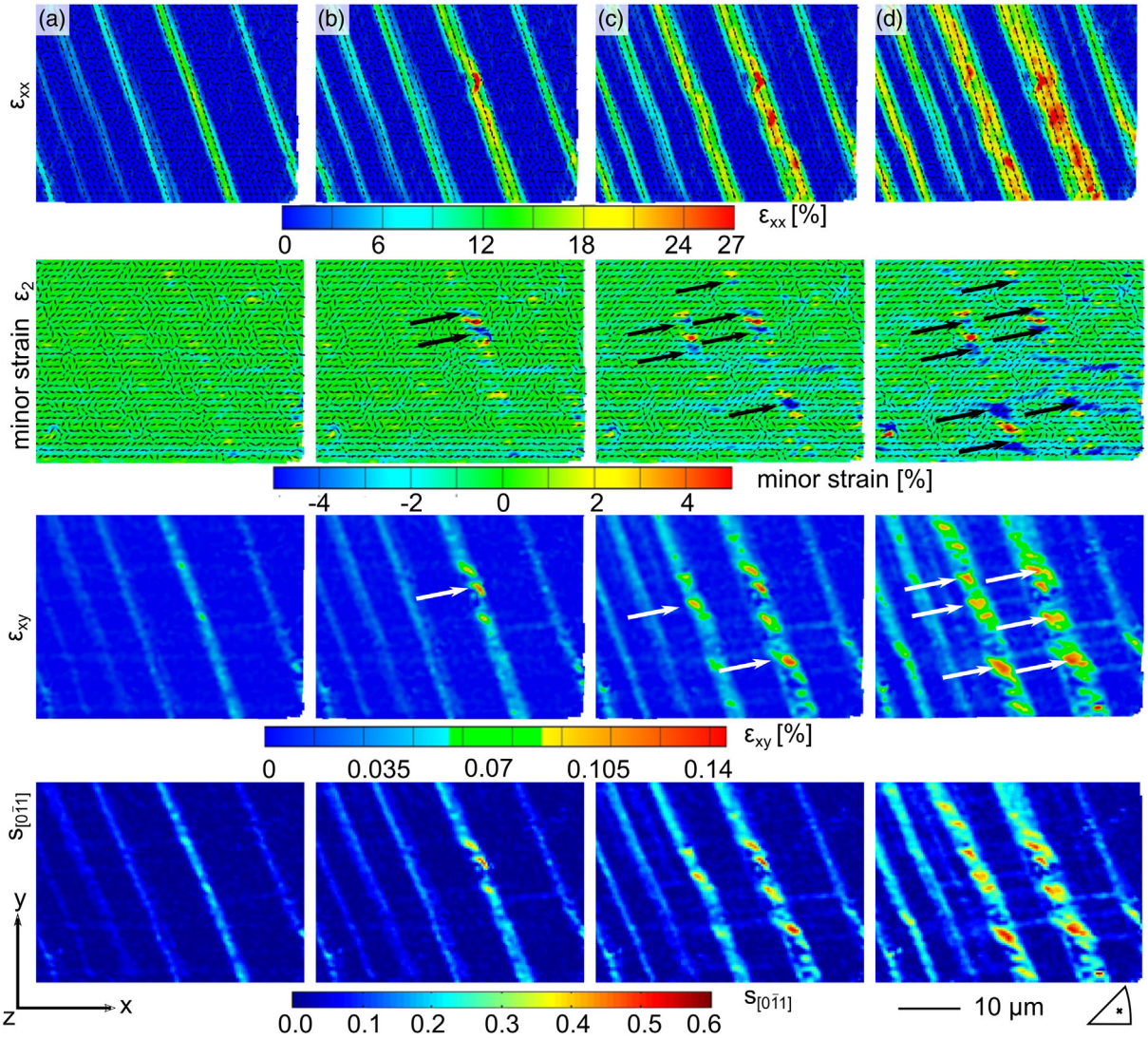

Figure 15. Evolution of the normal strain ε_{xx} (first row), the minor strain ε_2 (second row), the shear strain ε_{xy} (third row), and the absolute value of the magnitude of shear $s_{[0\bar{1}1]}$ (last row) of the AOI for a) $\varepsilon = 2\%$, b) $\varepsilon = 4\%$, c) $\varepsilon = 7\%$, and d) $\varepsilon = 12\%$. Adapted with permission.[141] Copyright 2020, Springer.

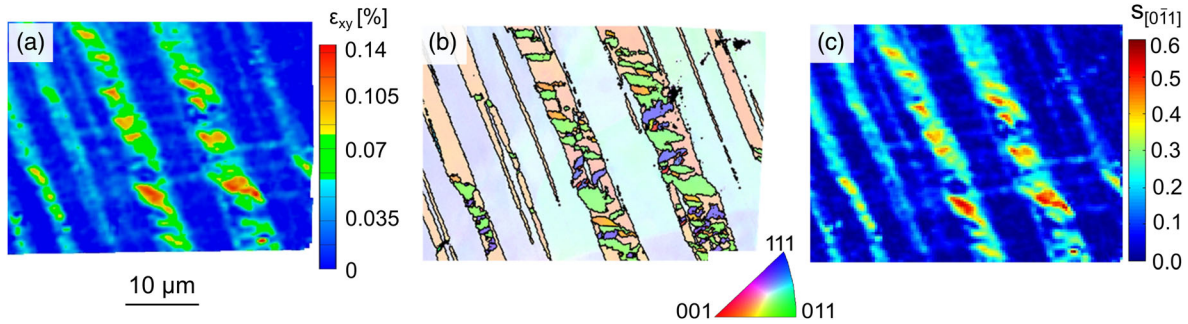

Figure 16. Local shear strain a) ε_{xx} and magnitude of shear c) $s_{[0\bar{1}1]}$ complemented by b) crystallographic orientation of γ-austenite (fcc), ε-martensite (hcp), and α'-martensite (bcc) at an applied strain of $\varepsilon = 15\%$. Adapted with permission.[141] Copyright 2020, Springer.

homogenous strain localizations within the deformation bands with values up to ε_{xx} 12% at an applied strain of $\varepsilon = 2$ %

At an applied strain of $\varepsilon = 4\%$, higher local strain values of up to $\varepsilon_{xx} = 27\%$ occur. These increased strain values ε_{xx} correlate with a butterfly contrast of negative and positive minor stain values ε_2 indicated by black arrows at $\varepsilon = 4\%$, 7%, and 12%, respectively. Moreover, the negative values of the minor strain ε_2 correspond to regions, which show high shear strain ε_{xy} marked by white arrows (Figure 15b–d, ε_{xy}, third row). The direction of minor strain can be described by an angle of 107° to the LA (small black arrows in Figure 15a–d, first row), which is in good agreement with the $[0\bar{1}1]$ direction, which is the cutting edge of the two activated SPs (111) and $(\bar{1}11)$.[160]

The absolute value of the magnitude of shear s was calculated with respect to the $[0\bar{1}1]$ direction shown in Figure 15a–d (last row). The shear is concentrated inside the deformation bands. A correlation with the developed microstructure shown in **Figure 16** allows a clear interpretation of the shear values. Absolute values of the magnitude of shear $s_{[0\bar{1}1]}$ between 0.2 and 0.3 were obtained in regions of deformation bands of ε-martensite without α'-martensite. This is in good agreement with theoretical considerations,[150,155,156] where the magnitude of shear for ε-martensite or individual SFs was given by $s_\varepsilon = \sqrt{2}/4 = 0.35$. Values of shear higher than 0.35 were observed in regions of α'-martensite islands.

However, a comparison of both the shear strain ε_{xy} and the absolute value of the magnitude of shear $s_{[0\bar{1}1]}$ with the map of crystallographic orientation demonstrates that differences occur between several martensite variants. Thus, α'-martensite variants with high shear strain ε_{xy} and high magnitude of shear $s_{[0\bar{1}1]}$ are accompanied by martensite grains with low shear strain values. The α'-martensite variants with high shear strain and high magnitude of shear, which correspond to the areas with negative minor strain ε_2 (see Figure 15b), are related to the martensitic variant shown in green color in Figure 16b. However, the green-colored martensite variant is always accompanied by a variant shown in orange color, which exhibits a twin orientation relationship (OR) to the green variant and is, in addition, related to lower shear strain and lower magnitude of shear. For interpretation of the local strain values and values of magnitude of shear, a detailed analysis of activated SSs was conducted based on crystallographic orientation data obtained from EBSD measurements. Thus, the activated SSs including trace angles of SPs and Burgers vectors at the surface as well as Schmid values μ for regular and partial dislocations were calculated for austenite and α'-martensite using the g-matrices of the individual grains. The results of the analysis of the SSs are shown in **Table 3**. However for the austenite (see Table 3a), the primary and secondary SSs are given both for regular and for partial dislocations, the ternary and quaternary SSs are given only for the regular

Table 3. Activated SSs of the investigated austenitic grain (a) and α'-martensite variants (b) in X5CrMnNi16-7-6 TRIP steel deformed in tension at RT (see Figure 16). (SS: SS; SP: slip plane; SD_{reg}: slip direction of regular dislocations; SD_{P1}: slip direction of leading partial dislocations, SD_{P2}: slip direction of trailing partial dislocations; ß: trace angle of the SP at the specimen surface). Adapted with permission.[141] Copyright 2020, Springer.

a)

			Primary SS			Secondary SS				Third SS	Fourth SS
SP	β	SD_{reg}	SD_{P1}	SD_{P2}	SD_{reg}	SD_{P1}	SD_{P2}	SD_{reg}	SD_{reg}
		$[\bar{1}01]$	$[\bar{2}11]$	$[\bar{1}\,\bar{1}\,2]$	$[101]$	$[1\bar{1}2]$	$[211]$	$[0\bar{1}\,\bar{1}]$	$[\bar{1}10]$
(111)	110°	0.48	0.45	0.36	—	—	—	—	—
$(\bar{1}11)$	105°	—	—	—	0.37	0.37	0.31	—	—
$(11\bar{1})$	25°	—	—	—	—	—	—	0.34	—
$(1\bar{1}1)$	6.5°	—	—	—	—	—	—	—	0.31

b)

Martensite variants		Primary SS				Secondary SS				
	μ	SP	β	SD	β	μ	SP	β	SD	β
α'_{i} (green)	0.48	$(\bar{1}01)$	110°	$[111]$	160°	0.46	(101)	156°	$[\bar{1}11]$	31°
α'_{ii} (orange)	0.49	$(\bar{1}01)$	112°	$[111]$	–28°	0.48	(101)	108°	$[\bar{1}11]$	157°
α'_{iii} (purple)	0.41	$(\bar{1}01)$	57°	$[111]$	–129°	0.34	$(0\bar{1}1)$	113°	$[11\bar{1}]$	113°

dislocations. As mentioned earlier, the trace angles of the primary and secondary SP are close together with $\beta = 110°$ and $\beta = 105°$, respectively. The α'-martensite grains are formed by the two-step shear mechanism including the leading partial dislocations (P1) of both systems. In addition, the activated SSs were calculated for the three identified martensite variants (green, orange, and purple) (see Table 3b).

It turned out that the α'-martensite variant α_i' (green color) was oriented to the parent austenite according to the Kurdjumov–Sachs' OR[165] (KS–OR), $(111)_\gamma||(\bar{1}01)_{\alpha'}$ and $[\bar{1}01]_\gamma|||[111]_{\alpha'}$, and primary SSs of austenite and α_i' martensite are compared. The other two variants (α_{ii}': orange and α_{iii}': purple) do not fulfil this relationship (see ref. [160]). Finally, there is no significant shear contribution of these variants in the observed x–y plane. These two orientations are twinning variants of the martensite variant α_i' with the highest magnitude of shear. However, the martensite variant α_{ii}' (orange) shows a high minor shear strain in comparison with martensite variant α_i', as it becomes obvious from Figure 16. Here, KS–OR is nearly fulfilled for the primary SS of the austenite and secondary SS of the martensite. In contrast, the martensite variant α_{iii}' (purple) exhibits no shear contribution at all—neither in major nor in minor strain in the plane of observation.

X5CrMnNi16-7-6 at 373 K and X5CrMnNi16-7-9 at RT. Both steels undergo the formation of SF-mediated twins either during loading at RT (X5CrMnNi16-7-9) or at 373 K (X5CrMnNi16-7-6). The magnitude of shear was calculated for the related SSs, as shown in **Figure 17**:1) primary SS $(111)[\bar{2}11]$ for X5CrMnNi16-7-6 at 373 K and 2) secondary SS $(11\bar{1})[1\bar{2}\,\bar{1}]$ for steel X5CrMnNi16-7-9 at RT.

In case of steel X5CrMnNi16-7-6 deformed at 373 K, the calculated magnitude of shear $s_{[\bar{2}11]}$ (Figure 14b) is between 0.2 and 0.3 for the formed twin bundles, as shown in Figure 17a. This is less than the theoretically calculated value $s_{twin} = 0.7$.[155,156] In addition, the regions between twin bundles exhibit values of magnitude of shear between 0.1 and 0.2.

In case of steel X5CrMnNi16-7-9 deformed at RT, the calculated magnitude of shear $s_{[1\bar{2}\bar{1}]}$ is about 0.75 for the thicker twin bundles (compare Figure 17c,d). This is in good agreement with the theoretical calculations.[155,156] However, smaller twin bundles exhibited significantly smaller values for magnitude of shear (0.25–0.5). One reason for the smaller magnitude of shear is that these regions were characterized by movement of regular dislocations, in particular for X5CrMnNi16-7-6 deformed at 373 K. Another reason could be that twins formed in these regions were in the size of nanotwins, which were nondetectable by EBSD. Similar to EBSD, these regions were below the resolution of DIC measurements. On the other hand, it is more likely that these regions exhibit also movement of partial dislocations. Here, the magnitude of shear in the order of 0.25 would fit very well. This agrees with Figure 12a, where parts of these bands are indexed by EBSD as hexagonal lattice structures are formed by SF on, in average each second, {111} lattice plane. This is even supported by the fact that twin bundles occurring in investigated TRIP/TWIP steels were formed by partial dislocations[141] and are, therefore, regarded as SF-mediated twins.

4.5. Discussion

The resolution of the SEM–DIC conducted in the case studies presented using the etching technique for the surface contrast pattern is well below 1 µm. Sutton et al.[12] demonstrated that the resolution of SEM–DIC is influenced by image shift and image distortions. Furthermore, parameters like 1) FOV, 2) image resolution, 3) magnification factor, 4) subset size, 5) image displacement accuracy, and 6) image speckle dimension have a high impact on the accuracy of DIC. Using these parameters, it is possible to calculate both the minimum object speckle dimension η_0 and the minimum spatial resolution $(l_0)_{min}$ achievable with DIC. The SEM–DIC conditions for the present investigations are shown in **Figure 18**. The FOV of 51 µm × 38 µm and the image resolution of 2048 pixels × 1538 pixels yield a resolution of 25 nm/pixel. Consequently, the subset size of 30 pixels results in a minimum spatial resolution of $(l_0)_{min} = 750$ nm (see Figure 18a,b). The etching pits caused by the etching techniques consist of about ten pixels, resulting in an object speckle dimension of $\eta_0 = 250$ nm. Thus, a spatial resolution of ≤ 750 nm is possible, considering the additional subpixel algorithm implemented in the DIC software. Deformation bands with thickness of 500 nm were resolved by the applied DIC, as shown in Figure 10a,b. In Figure 18c,d, the minimum spatial resolution of $(l_0)_{min} = 750$ nm is in the range of the thickness of deformation bands (slip bands) developed in steel X5CrMnNi16-7-9 at tensile strain $\varepsilon = 2\%$ at 473 K.

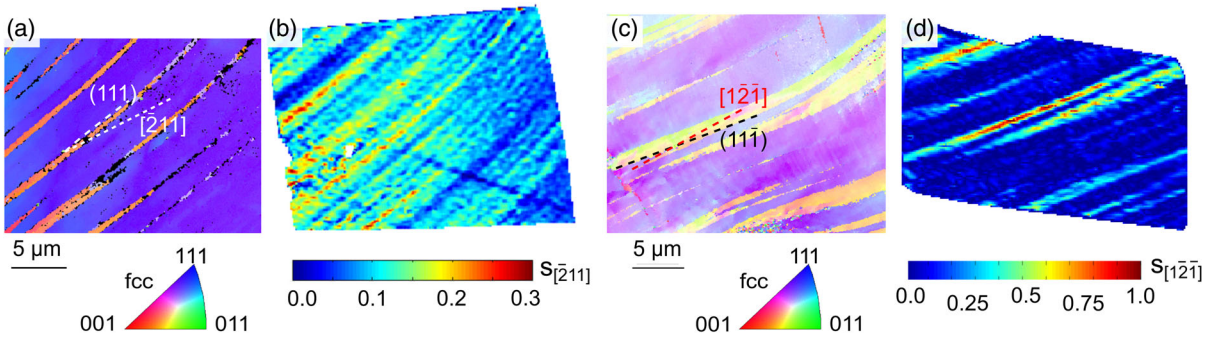

Figure 17. a,b) Steel X5CrMnNi16-7-6 deformed at 373 K and c,d) steel X5CrMnNi16-7-9 deformed at RT. a,c) Crystallographic orientation map of the AOI in IPF coloring with respect to the LA. The twin systems are indicated by twin planes and shear directions. b,d) Magnitude of shear calculated in the twin shear directions $[\bar{2}11]$ (b) and $[1\bar{2}\,\bar{1}]$ (d), respectively. Adapted with permission.[141] Copyright 2020, Springer.

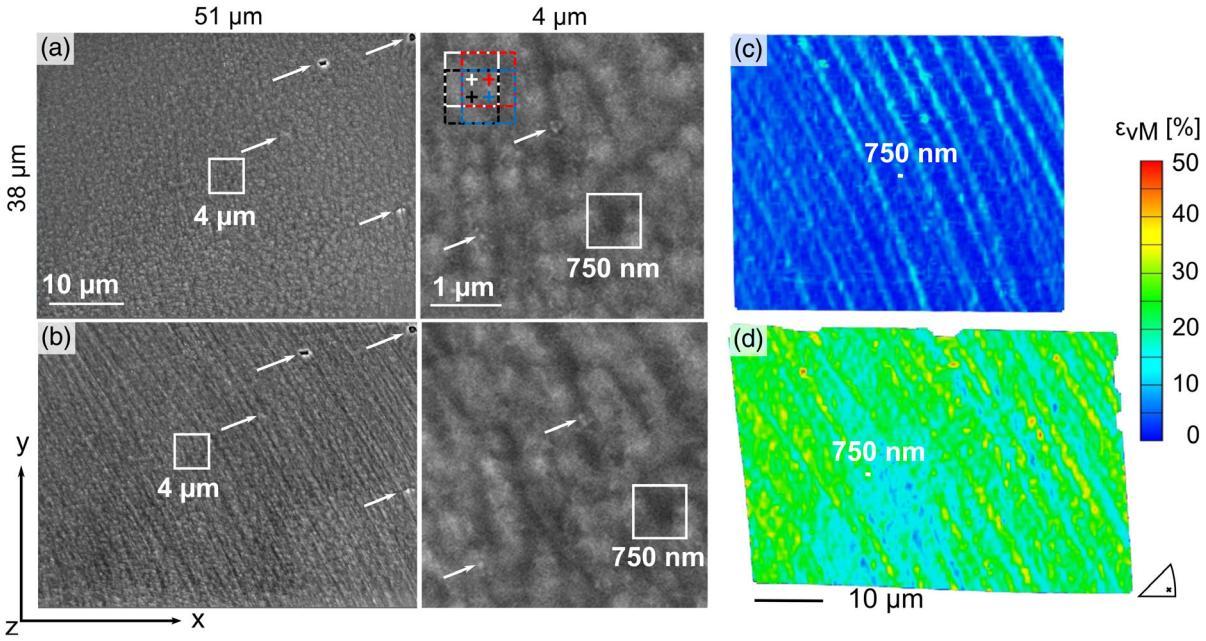

Figure 18. Resolution of SEM–DIC exemplarily shown for steel X5CrMnNi16-7-9 under quasistatic tensile deformation at 473 K. a) Reference image at $e = 0\%$ with an FOV of 51 µm × 38 µm, the subset size of 30 pxl × 30 pxl, and 10 pxl distance of measuring points. b) Same FOV at $e = 15\%$. Obviously identical areas in (a) and (b) are marked by white arrows. c,d) Local strain fields in terms of von Mises equivalent strain at $e = 2\%$ (c) and $e = 15\%$ (d). Minimum achievable spatial resolution of 750 nm is indicated by a white horizontal bar in (c) and (d). Adapted with permission.[141] Copyright 2020, Springer.

The resolution of SEM–DIC is also influenced by image distortions. Kammers et al.[27] showed that the strain error due to image distortions can be as large as 0.01. The image distortion is severely influenced by the image capturing time in combination with stress relaxations during quasi-in situ testing, where deformation is interrupted at defined strain intervals. As mentioned by Kammers et al.,[27] image distortion can be neglected for capturing times less than 120 s. In the present case, the image capturing time was 67 s and relaxation time was 90 s for each deformation interval. In the present case studies, no distortion corrections were applied, as obviously in none of the analyzed strain fields (ε_{xx}, ε_{yy}, ε_{xy}) systematically over- or underestimated strain regions were observed.

Besides the high lateral resolution of µDIC, the absolute resolution of strain is also reasonably good, considering that only in-plane displacements were measured by the SEM–DIC, although definitely out-of-plane displacements also occur in regions of deformation bands and α'-martensite grains. The achieved absolute resolution of strain is about 0.001, which is perfectly demonstrated by the calculated magnitude of shear. Moreover, the orientation dependence of the magnitude of shear for different α'-martensite variants was demonstrated.

The applied etching technique, resulting in submicrometer SEM–DIC, is a robust contrasting method, which covers a large variety of testing conditions even at elevated temperatures. In particular, the tensile tests conducted on steel X5-CrMnNi-16-7-9 at 473 K did not reveal significantly higher drift distortions or a loss of the spatial resolution (see Figure 18c,d).

However, the grain size has a significant influence on the detectability of strain localizations on the microscopic level in terms of deformation bands or martensitic grains. Thus, the results of submicrometer SEM–DIC presented here were obtained on high-alloy CrMnNi cast steels with a large grain size in the range from 0.05 up to 2 mm. The strain localizations start either in the interior of a grain on pre-existing lattice defects such as SFs, SF tetrahedrons, and subgrain boundaries and/or at large-angle grain boundaries. A majority of these bands were so-called single-ended bands as they did not cross the entire austenitic grains.

A reduction in the austenitic grain size will result in so-called double-ended bands crossing the entire grains. Finally, this yields either the activation of parallel SPs or a slip transition into neighboring grains. Moreover, the thickness of deformation bands will reduce and, therefore, the resolution of individual martensite variants becomes more difficult (see ref. [141]). Here, a much finer object speckle dimension size in the range of few nanometers would be helpful.

5. Perspectives and Conclusion

The Review presented a comprehensive overview on DIC with respect to both development of theoretical background and applications in the field of MSE starting from the invention of DIC in the 1980s to the present.

The SEM–DIC results presented in the article for high-strength steels showed that the DIC method can be used to determine the shear contribution of individual microstructural constituents to the global plastic deformation at a high lateral resolution. It was demonstrated on the example of high-alloy

CrMnNi-cast TRIP/TWIP steels that the combination of in situ deformation in SEM with well-contrasted specimen surfaces and high-resolution SE contrast images is able to detect strain localizations in the submicrometer range. Moreover, it was shown by the calculated magnitude of shear that the formation of SFs (deformation bands, ε-martensite) and α'-martensite results in different contributions to the plastic deformation. The shear values obtained for deformation bands agree with theoretical consideration in the order of $s = 0.35$. Only α'-martensite variants with a specific crystallographic orientation fulfilling the Kurdjumov–Sachs relationship contribute a significantly higher amount to the global strain.

In future, the high-resolution SEM–DIC can be applied 1) for other loading scenarios, 2) investigations on other materials with complex deformation mechanisms including (martensitic) phase transformation, and 3) in combination with other complementary in situ characterization techniques such as AE measurements. In particular, the combination of AE measurements with the submicrometer DIC would provide a deeper understanding of strain fields occurring during different microstructural processes, supporting computational simulation of material behavior under mechanical loading.

Supporting Information

Supporting Information is available from the Wiley Online Library or from the author.

Acknowledgements

The financial support of the CRC799 TRIP matrix composites by the German Research Foundation (Deutsche Forschungsgemeinschaft) under project ID 54434667 is gratefully acknowledged (subproject B5). The authors thank K. Zuber for preparation of the specimens for scanning electron microscopy (SEM) investigations. C. Segel is acknowledged for assistance with in situ deformations in the SEM and digital image correlation (DIC) calculations. Moreover, Chemnitzer Werkzeugmechanik GmbH Chemnitz, Germany) and Kammrath&Weiss company (Dortmund, Germany) are gratefully acknowledged for their support regarding DIC based on SEM micrographs and the mechanical tests.

Open access funding enabled and organized by Projekt DEAL.

Conflict of Interest

The authors declare no conflict of interest.

Keywords

digital image correlation, magnitude of shear, scanning electron microscopy, strain fields, strain localizations

Received: November 23, 2020
Revised: February 10, 2021
Published online:

[1] A. Considère, *Annales des Ponts et Chaussées*, **1885**, *9*, 574.
[2] Y. Estrin, *Solid State Phenomena* **1988**, *3–4*, 417.
[3] Y. Estrin, L. P. Kubin, *Mater. Sci. Eng., A* **1991**, *137*, 125.
[4] J. R. Rice, *Theo. Appl. Mech.* **1976**, *1*, 207.
[5] Y. Bréchet, F. Louchet, *Solid State Phenomena* **1988**, *3–4*, 347.
[6] S. D. Antolovich, R. W. Armstrong, *Prog. Mater. Sci.* **2014**, *59*, 1.
[7] *Advancements in Optical Methods & Digital Image Correlation in Experimental Mechanics, Volume 3: Proceedings of the 2019 Annual Conf. on Experimental and Applied Mechanics* (Eds.: M.-T. Lin, C. Sciammarella, H.D. Espinosa, C. Furlong, L. Lamberti, P. Reu, M. Sutton, C.-H. Hwang), Springer Nature, Cham **2019**.
[8] P. Jacquot, J.-M. Fournier, *Interferometry in Speckle Light: Theory and Applications. Micromechanical Application of Digital Image Correlation Technique*, Springer Berlin Heidelberg, Berlin/Heidelberg **2000**.
[9] E. Soppa, P. Doumalin, P. Binkele, T. Wiesendanger, M. Bornert, S. Schmauder, *Comp. Mater. Sci.* **2001**, *21*, 261.
[10] A. Tatschl, O. Kolednik, *Mater. Sci. Eng., A* **2003**, *339*, 265.
[11] M. A. Sutton, N. Li, D. Garcia, N. Cornille, J. J. Orteu, S. R. McNeill, H. W. Schreier, X. Hi, *Meas. Sci. Technol.* **2006**, *17*, 2613.
[12] M. A. Sutton, N. Li, D. C. Joy, A. P. Reynolds, X. Li, *Exp. Mech.* **2007**, *47*, 289.
[13] A. M. Korsunsky, M. Sebastiani, E. Bemporad, *Mater. Lett.* **2009**, *63*, 1961.
[14] M. Sebastiani, C. Eberl, E. Bemporad, G. M. Pharr, *Mater. Sci. Eng., A* **2011**, *528*, 7901.
[15] M. Krottenthaler, C. Schmid, J. Schaufler, K. Durst, M. Göken, *Surf. Coat. Technol.* **2013**, *215*, 247.
[16] S. Cho, I. Chasiotis, T. A. Friedmann, J. P. Sullivan, *J. Micromech. Microeng.* **2005**, *15*, 728.
[17] S. W. Cho, K. Jonnalagadda, I. Chasiotis, *Fat. Frac. Eng. Mat. Struct.* **2007**, *30*, 21.
[18] S. W. Cho, I. Chasiotis, *Exp. Mech.* **2007**, *47*, 37.
[19] Z.-H. Xu, M. A. Sutton, X. Li, *Acta Mater.* **2008**, *56*, 6304.
[20] K. Han, M. Ciccotti, S. Roux, *Europhys. Lett.* **2010**, *89*, 66003.
[21] X. Li, W. Xu, M. A. Sutton, M. Mello, *Mater. Sci. Technol.* **2013**, *22*, 835.
[22] T. S. Smith, B. K. Bay, M. M. Rashid, *Exp. Mech.* **2002**, *42*, 272.
[23] I. Jandejsek, O. Jiroušek, D. Vavřík, *Proced. Eng.* **2011**, *10*, 1730.
[24] J. Rannou, N. Limodin, J. Réthoré, A. Gravouil, W. Ludwig, M.-C. Baïetto-Dubourg, J.-Y. Buffière, A. Combescure, F. Hild, S. Roux, *Comp. Meth. Appl. Mech. Eng.* **2010**, *199*, 1307.
[25] C. Gammer, C. Ophus, T. C. Pekin, J. Eckert, A. M. Minor, *Appl. Phys. Lett.* **2018**, *112*, 171905.
[26] H. W. Schreier, M. A. Sutton, *Exp. Mech.* **2002**, *42*, 303.
[27] A. D. Kammers, S. Daly, *Exp. Mech.* **2013**, *53*, 1743.
[28] G. B. Olson, *Science (Washington, DC, U.S.)* **2000**, *288*, 993.
[29] D. L. McDowell, F. P. E. Dunne, *Adv. Very High Cycle Fatig.* **2010**, *32*, 1521.
[30] C. C. Tasan, M. Diehl, D. Yan, C. Zambaldi, P. Shanthraj, F. Roters, D. Raabe, *Acta Mater.* **2014**, *81*, 386.
[31] F. Roters, P. Eisenlohr, C. Kords, D. D. Tjahjanto, M. Diehl, D. Raabe, *Proc. IUTAM* **2012**, *3*, 3.
[32] W. Song, W. Bleck, U. Prahl, in *Proc. of the 3rd World Congress on Integrated Computational Materials Engineering* (Eds.: W. Poole, S. Christensen, S. Kalidindi, A. Luo, J. Madison, D. Raabe, X. Sun), John Wiley & Sons, Inc, Hoboken, NJ **2015**, pp. 39–46.
[33] J. Hosdez, M. Langlois, J.-F. Witz, N. Limodin, D. Najjar, E. Charkaluk, P. Osmond, A. Forre, F. Szmytka, *Int. J. Solids Struct.* **2019**, *171*, 92.
[34] *Full-field measurements and identification in solid mechanics: Chapter 6: Digital Image Correlation*, 1st ed. (Eds.: M. Grediac, F. Hild), John Wiley & Sons, Inc, Hoboken, NJ **2013**.
[35] T. D. Dudderar, *Exp. Mech.* **1969**, *9*, 281.
[36] J. A. Leendertz, *J. Phys. E* **1970**, *3*, 214.
[37] D. Post, W. A. Baracat, *Exp. Mech.* **1981**, *21*, 100.
[38] C. A. Walker, *Exp. Mech.* **1994**, *34*, 281.

[39] J. Fang, F.-L. Dai, *Exp. Mech.* **1991**, *31*, 163.
[40] M. A. Sutton, W. J. Wolters, W. H. Peters, W. F. Ranson, S. R. McNeill, *Image Vision Comput.* **1983**, *1*, 133.
[41] T. C. Chu, W. F. Ranson, M. A. Sutton, W. H. Peters, *Exp. Mech.* **1985**, *25*, 232.
[42] A. Kurtovic, T. Niendorf, T. Hausöl, H. W. Höppel, M. Göken, H. J. Maier, *Scripta Mater.*, **2013**, *68*, 809.
[43] M. D. Sangid, G. J. Pataky, H. Sehitoglu, R. G. Rateick, T. Niendorf, H. J. Maier, *Acta Mater.*, **2011**, *59*, 7340.
[44] B. Gorny, T. Niendorf, J. Lackmann, M. Thoene, T. Troester, H. J. Maier, *Mater. Sci. Eng., A*, **2011**, *528*, 7962.
[45] C. Efstathiou, H. Sehitoglu, J. Lambros, *Int. J. Plast.* **2010**, *26*, 93.
[46] M. A. Sutton, N. Li, D. Garcia, N. Cornille, J. J. Orteu, S. R. McNeill, H. W. Schreier, X. Li, A. P. Reynolds, *Exp. Mech.* **2007**, *47*, 789.
[47] L. Bodelot, L. Sabatier, E. Charkaluk, P. Dufrénoy, *Mater. Sci. Eng., A* **2009**, *501*, 52.
[48] R. Seghir, J. F. Witz, L. Bodelot, E. Charkaluk, P. Dufrenoy, *Proc. Eng.* **2011**, *10*, 3596.
[49] R. Seghir, L. Bodelot, E. Charkaluk, P. Dufrénoy, *Comput. Mater. Sci.* **2012**, *53*, 464.
[50] R. Seghir, J.-F. Witz, E. Charkaluk, P. Dufrénoy, *Mech. Ind.* **2012**, *13*, 395.
[51] A. Ahadi, Q. Sun, *Scr. Mater.* **2016**, *113*, 171.
[52] A. Maynadier, M. Poncelet, K. Lavernhe-Taillard, S. Roux, *Exp. Mech.* **2012**, *52*, 241.
[53] B. Pan, L. Yu, Q. Zhang, *Sci. China Technol. Sci.* **2018**, *61*, 2.
[54] A. Giachetti, *Image Vis. Comput.* **2000**, *18*, 247.
[55] W. Tong, *Strain* **2005**, *41*, 167.
[56] B. Pan, K. Qian, H. Xie, A. Asundi, *Meas. Sci. Technol.* **2009**, *20*, 62001.
[57] B. Pan, H. Xie, B. Xu, F. Dai, *Meas. Sci. Technol.* **2006**, *17*, 1615.
[58] H. A. Bruck, S. R. McNeill, M. A. Sutton, W. H. Peters, *Exp. Mech.* **1989**, 261.
[59] C. Q. Davis, *Opt. Eng.* **1998**, *37*, 1290.
[60] F. Bourdin, J. C. Stinville, M. P. Echlin, P. G. Callahan, W. C. Lenthe, C. J. Torbet, D. Texier, F. Bridier, J. Cormier, P. Villechaise, T. M. Pollock, V. Valle, *Acta Mater.* **2018**, *157*, 307.
[61] J. C. Stinville, P. G. Callahan, M. A. Charpagne, M. P. Echlin, V. Valle, T. M. Pollock, *Acta Mater.* **2020**, *186*, 172.
[62] Y. Luo, J. Ruff, R. Ray, Y. Gu, H. J. Ploehn, W. A. Scrivens, *Chem. Mater.* **2005**, *17*, 5014.
[63] W. A. Scrivens, Y. Luo, M. A. Sutton, S. A. Collette, M. L. Myrick, P. Miney, P. E. Colavita, A. P. Reynolds, X. Li, *Exp. Mech.*, **2007**, *47*, 63.
[64] M. A. Tschopp, B. B. Bartha, W. J. Porter, P. T. Murray, S. B. Fairchild, *Metall. Mater. Trans. A* **2009**, *40*, 2363.
[65] J. L. Walley, R. Wheeler, M. D. Uchic, M. J. Mills, *Exp. Mech.* **2012**, *52*, 405.
[66] N. Biery, M. de Graef, T. M. Pollock, *Metall. Mater. Trans. A* **2003**, *34*, 2301.
[67] N. B. Amar, P. V. de Lesegno, A. Beghdadi, *Local Strain and Temperature Measurements*, **1999**, p. 138.
[68] H. Ghadbeigi, C. Pinna, S. Celotto, *Mater. Sci. Eng., A* **2013**, *588*, 420.
[69] J. C. Stinville, N. Vanderesse, F. Bridier, P. Bocher, T. M. Pollock, *Acta Mater.* **2015**, *98*, 29.
[70] J. Jiang, T. Zhang, F. P. E. Dunne, T. B. Britton, *Proc. Math. Phys. Eng. Sci.* **2016**, *472*, 20150690.
[71] J. Karlsson, T. Sjögren, A. Snis, H. Engqvist, J. Lausmaa, *Mater. Sci. Eng., A* **2014**, *618*, 456.
[72] J. Lubliner, *Plasticity Theory*, Dover Publications, Newburyport **2013**.
[73] GOM, *Optical Measuring Techniques: ARAMIS, Software Manual*, GOM, Braunschweig **2008**.
[74] J. Zhao, Y. Sang, F. Duan, *Eng. Rep.* **2019**, *1*, 323.
[75] B. Pan, *Opt. Las. Eng.* **2013**, *51*, 1161.
[76] G. Vendroux, W. G. Knauss, *Exp. Mech.* **1998**, *38*, 86.
[77] H. Lu, P. D. Cary, *Exp. Mech.* **2000**, *40*, 393.
[78] B. Pan, Z. Lu, H. Xie, *Opt. Las. Eng.* **2010**, *48*, 469.
[79] Z. Gao, X. Xu, Y. Su, Q. Zhang, *Opt. Las. Eng.* **2016**, *81*, 46.
[80] F. Delaire, J. L. Raphanel, C. Rey, *Acta Mater.* **2000**, *48*, 1075.
[81] A. D. Kammers, S. Daly, *Exp. Mech.* **2013**, *53*, 1333.
[82] F. Di Gioacchino, J. Quinta da Fonseca, *Exp. Mech.* **2013**, *53*, 743.
[83] E. Heripre, M. Dexet, J. Crepin, L. Gelebart, A. Roos, *Inter. J. Plastic.* **2007**, *23*, 1512.
[84] C. C. Tasan, J. P. M. Hoefnagels, M. Diehl, D. Yan, F. Roters, D. Raabe, *Inter. J. Plastic.* **2014**, *63*, 198.
[85] F. Di Gioacchino, J. Quinta da Fonseca, *Inter. J. Plastic.* **2015**, *74*, 92.
[86] B. Winiarski, G. S. Schajer, P. J. Withers, *Exp. Mech.* **2012**, *52*, 793.
[87] A. D. Kammers, S. Daly, *Meas. Sci. Technol.* **2011**, *22*, 125501.
[88] D. Raabe, M. Sachtleber, Z. Zhao, F. Roters, S. Zaefferer, *Acta Mater.* **2001**, *49*, 3433.
[89] M. Sachtleber, Z. Zhao, D. Raabe, *Mater. Sci. Eng., A* **2002**, *336*, 81.
[90] B. M. Schroeter, D. L. Mc Dowell, *Inter. J. Plastic.* **2003**, *19*, 1355.
[91] N. Zhang, W. Tong, *Inter. J. Plastic.* **2004**, *20*, 523.
[92] J. Q. da Fonseca, P. M. Mummery, P. J. Withers, *J. Microsc.* **2005**, *218*, 9.
[93] J. Zdunek, T. Brynk, J. Mizera, Z. Pakieła, K. J. Kurzydłowski, *Mater. Charact.* **2008**, *59*, 1429.
[94] M. Eskandari, M. R. Yadegari-Dehnavi, A. Zarei-Hanzaki, M. A. Mohtadi-Bonab, R. Basu, J. A. Szpunar, *Opt. Las. Eng.* **2015**, *67*, 1.
[95] W. Chow, D. Solas, G. Puel, T. Baudin, V. Aubin, *J. Mater. Sci.* **2016**, *51*, 1234.
[96] A. E. Bartali, V. Aubin, S. Degallaix, *Fatigue Fract. Eng. Mater. Struct.* **2008**, *31*, 137.
[97] A. E. Bartali, V. Aubin, S. Degallaix, *Adv. Very High Cycle Fatigue* **2009**, *31*, 2049.
[98] T. Niendorf, J. Dadda, D. Canadinc, H. J. Maier, I. Karaman, *Mater. Sci. Eng., A* **2009**, *517*, 225.
[99] W. G. Mao, J. Chen, M. S. Si, R. F. Zhang, Q. S. Ma, D. N. Fang, X. Chen, *Mater. Sci. Eng., A*, **2016**, *665*, 26.
[100] A. Chrysochoos, B. Berthel, F. Latourte, A. Galtier, S. Pagano, B. Wattrisse, *J. Strain Analy. Eng. Design* **2008**, *43*, 411.
[101] G. Besnard, F. Hild, S. Roux, *Exp. Mech.* **2006**, *46*, 789.
[102] S. Avril, F. Pierron, M. A. Sutton, J. Yan, *Mech. Mater.* **2008**, *40*, 729.
[103] Z. Zhao, M. Ramesh, D. Raabe, A. M. Cuitio, R. Radovitzky, *Int. J. Plastic.* **2008**, *24*, 2278.
[104] A. Saai, H. Louche, L. Tabourot, H. J. Chang, *Mech. Mater.* **2010**, *42*, 275.
[105] J. Carroll, W. Abuzaid, J. Lambros, H. Sehitoglu, *Rev. Sci. Instrum.* **2010**, *81*, 83703.
[106] W. Abuzaid, H. Sehitoglu, J. Lambros, *Mater. Sci. Eng., A* **2013**, *561*, 507.
[107] H. Jin, W.-Y. Lu, J. Korellis, *J. Strain Analy. Eng. Design* **2008**, *43*, 719.
[108] C. C. Tasan, J. P. M. Hoefnagels, M. G. D. Geers, *Scr. Mater.* **2010**, *62*, 835.
[109] F. Schäfer, P. Grünewald, L. Weiter, M. Thielen, M. Marx, C. Motz, in *Conf. Paper, 14th Conf. Metallography*, Leoben **2014**, https://doi.org/10.13140/2.1.1410.2720.
[110] J. C. Pina, S. Shafqat, V. G. Kouznetsova, J. P. M. Hoefnagels, M. G. D. Geers, *Mater. Sci. Eng., A*, **2016**, *658*, 439.
[111] A. Tatschl, O. Kolednik, *Mater. Sci. Eng., A*, **2004**, *364*, 384.
[112] J. Kang, Y. Ososkov, J. D. Embury, D. S. Wilkinson, *Scr. Mater.* **2007**, *56*, 999.
[113] H. Ghadbeigi, C. Pinna, S. Celotto, J. R. Yates, *Mater. Sci. Eng., A* **2010**, *527*, 5026.
[114] J. C. Stinville, M. P. Echlin, D. Texier, F. Bridier, P. Bocher, T. M. Pollock, *Exp. Mech.* **2016**, *56*, 197.

[115] J. C. Stinville, P. G. Callahan, M. A. Charpagne, M. P. Echlin, V. Valle, T. M. Pollock, *Acta Mater.* **2019**, *186*, 172.
[116] J. C. Stinville, T. Francis, A. T. Polonsky, C. J. Torbet, M. A. Charpagne, Z. Chen, G. H. Balbus, F. Bourdin, V. Valle, P. G. Callahan, M. P. Echlin, T. M. Pollock, *Exp. Mech.* **2010**, *56*, 10.
[117] C. Lineau, P. V. de Lesegno, C. Rey, T. Chauveau, *Local Strain Temp. Measur.* **1999**, 159.
[118] T. Hoc, C. Rey, *Scr. Mater.* **2000**, *42*, 1053.
[119] T. Hoc, C. Rey, *Scr. Mater.* **2000**, *42*, 749.
[120] S. Bugat, J. Besson, A.-F. Gourgues, F. N'Guyen, A. Pineau, *Mater. Sci. Eng., A*, **2001**, *317*, 32.
[121] T. Hoc, J. Crepin, L. Gelebart, A. Zaoui, *Acta Mater.* **2003**, *51*, 5477.
[122] H. A. Crostack, G. Fischer, E. Soppa, S. Schmauder, Y. L. Liu, *J. Microsc.* **2001**, *201*, 171.
[123] J. Marteau, H. Haddadi, S. Bouvier, *Exp. Mech.* **2013**, *53*, 427.
[124] Q. Han, Y. Kang, P. D. Hodgson, N. Stanford, *Scr. Mater.* **2013**, *69*, 13.
[125] N. Li, M. A. Sutton, X. Li, H. W. Schreier, *Exp. Mech.* **2008**, *48*, 635.
[126] S.-H. Joo, J. K. Lee, J.-M. Koo, S. Lee, D.-W. Suh, H. S. Kim, *Scr. Mater.* **2013**, *68*, 245.
[127] M. Kimiecik, J. W. Jones, S. Daly, *Mater. Lett.* **2013**, *95*, 25.
[128] H. Lim, J. D. Carroll, C. C. Battaile, T. E. Buchheit, B. L. Boyce, C. R. Weinberger, *Int. J. Plastic.* **2014**, *60*, 1.
[129] Y. Guan, B. Chen, J. Zou, T. B. Britton, J. Jiang, F. P. E. Dunne, *Int. J. Plastic.* **2017**, *88*, 70.
[130] O. Grässel, L. Krüger, G. Frommeyer, L. W. Meyer, *Int. J. Plastic.* **2000**, *16*, 1391.
[131] C. Herrera, D. Ponge, D. Raabe, *Acta Mater.* **2011**, *59*, 4653.
[132] B. C. de Cooman, J. Kim, S. Lee, *Scr. Mater.* **2012**, *66*, 986.
[133] G. Frommeyer, U. Brüx, P. Neumann, *ISIJ Int.*, **2003**, *43*, 438.
[134] A. Weiss, H. Gutte, M. Radtke, P. Scheller, Nichtrostender austenitischer Stahlformguss, Verfahren zu dessen Herstellung, und seine Verwendung C22C 38/00 (2006.01) C21D 8/00 (2006.01) (WO 2008/009722 A1), **2007**.
[135] A. Jahn, A. Kovalev, A. Weiß, S. Wolf, L. Krüger, P. R. Scheller, *Steel Res. Int.* **2011**, *82*, 39.
[136] L. Krüger, S. Wolf, S. Martin, U. Martin, A. Jahn, A. Weiß, P. R. Scheller, *Steel Res. Int.* **2011**, *82*, 1087.
[137] D. Kulawinski, K. Nagel, S. Henkel, P. Hübner, H. Fischer, M. Kuna, H. Biermann, *Eng. Fract. Mech.* **2011**, *78*, 1684.
[138] S. Wolf, S. Martin, L. Krüger, U. Martin, U. Lorenz, *Steel Res. Int.* **2012**, *83*, 529.
[139] A. Glage, A. Weidner, H. Biermann, *Steel Res. Int.* **2011**, *82*, 1040.
[140] H. Biermann, J. Solarek, A. Weidner, *Steel Res. Int.* **2012**, *83*, 512.
[141] A. Weidner, *Deformation Processes in TRIP/TWIP Steels: In SITU Characterization Techniques*, Springer Series in Materials Science, Springer, Cham **2020**.
[142] A. Vinogradov, A. Lazarev, M. Linderov, A. Weidner, H. Biermann, *Acta Mater.* **2013**, *61*, 2434.
[143] M. Linderov, C. Segel, A. Weidner, H. Biermann, A. Vinogradov, *Mater. Sci. Eng., A* **2014**, *597*, 183.
[144] M. L. Linderov, C. Segel, A. Weidner, H. Biermann, A. Y. Vinogradov, *Phys. Met. Metallogr.* **2018**, *119*, 388.
[145] A. Weidner, R. Lehnert, H. Biermann, *Scanning Electron Microscopy and Complementary In Situ Characterization Techniques for Characterization of Deformation and Damage Processes*, Springer Series in Materials Science, Springer, Cham **2020**.
[146] S. Martin, S. Wolf, U. Martin, L. Krüger, *Solid State Phenomena*, **2011**, *172–174*, 172.
[147] A. Jahn, A. Kovalev, A. Weiß, P. R. Scheller, *Steel Res. Int.* **2011**, *82*, 1108.
[148] D. Rafaja, C. Krbetschek, D. Borisova, G. Schreiber, V. Klemm, *Thin Solid Films* **2013**, *530*, 105.
[149] D. Rafaja, C. Krbetschek, C. Ullrich, S. Martin, *J. Appl. Crystallogr.*, **2014**, *47*, 936.
[150] G. B. Olson, M. Cohen, *J. Less Common Metals*, **1972**, *28*, 107.
[151] A. Weidner, S. Martin, V. Klemm, U. Martin, H. Biermann, *Scr. Mater.* **2011**, *64*, 513.
[152] S. Martin, C. Ullrich, D. Šimek, U. Martin, D. Rafaja, *J. Appl. Crystallogr.* **2011**, *44*, 779.
[153] S. Ackermann, S. Martin, M. R. Schwarz, C. Schimpf, D. Kulawinski, C. Lathe, S. Henkel, D. Rafaja, H. Biermann, A. Weidner, *Metall. Mater. Trans. A* **2016**, *47*, 95.
[154] G. B. Olson, M. Cohen, *Metall. Trans. A* **1975**, *6*, 791.
[155] H. Schumann, *Krist. Technol.* **1976**, *11*, 663.
[156] H. Schumann, *Krist. Technol.* **1977**, *12*, 363.
[157] H. Na, S. Nambu, M. Ojima, J. Inoue, T. Koseki, *Scr. Mater.* **2013**, *69*, 793.
[158] A. Ramazani, Z. Ebrahimi, U. Prahl, *Comput. Mater. Sci.* **2014**, *87*, 241.
[159] L. Remy, *Acta Metall.* **1977**, *25*, 173.
[160] A. Weidner, C. Segel, H. Biermann, *Mater. Lett.* **2015**, *143*, 155.
[161] S. Martin, S. Wolf, U. Martin, L. Krüger, D. Rafaja, *Metall. Mater. Trans. A* **2016**, *47*, 49.
[162] D. Borisova, V. Klemm, S. Martin, S. Wolf, D. Rafaja, *Adv. Eng. Mater.* **2013**, *15*, 571.
[163] C. Cayron, *Acta Crystallogr. A* **2013**, *69*, 498.
[164] L. Bracke, L. Kestens, J. Penning, *Scr. Mater.* **2007**, *57*, 385.
[165] C. W. Sinclair, R. G. Hoagland, *Acta Mater.* **2008**, *56*, 4160.
[166] C. W. Sinclair, *J. Phys.: Conf. Ser.* **2010**, *240*, 12105.
[167] G. Kurdjumov, G. Sachs, *Zeitschrift für Physik* **1930**, *64*, 325.
[168] A. Weidner, H. Biermann, *JOM* **2015**, *67*, 1729.

Anja Weidner has been senior scientist at the Institute of Materials Engineering at the Technische Universität Bergakademie Freiberg, Germany, since 2009. She studied Materials Science in Freiberg and received her doctorate and habilitation. Her primary research interests focus on plasticity, fatigue, and related microstructural analysis of materials. Her particular interests are related to the application of complementary in situ characterization techniques for better understanding of kinetics of deformation and damage processes. To date she has authored or coauthored over 100 peer-reviewed publications.

Horst Biermann has been University professor for Materials Engineering and head of the Institute of Materials Engineering at the Technische Universität Bergakademie Freiberg, Germany, since 2000. He studied Materials Science at the University of Erlangen-Nuremberg and received his doctorate and habilitation. His fields of work include plasticity, fatigue, as well as surface engineering with about 400 publications as author or coauthor.